National Library of Canada
Acquisitions and Bibliographic Services Branch
395 Wellington Street
Ottawa, Ontario
K1A 0N4

Bibliothèque nationale du Canada
Direction des acquisitions et des services bibliographiques
395, rue Wellington
Ottawa (Ontario)
K1A 0N4

Your file Votre référence

Our file Notre référence

NOTICE

The quality of this microform is heavily dependent upon the quality of the original thesis submitted for microfilming. Every effort has been made to ensure the highest quality of reproduction possible.

If pages are missing, contact the university which granted the degree.

Some pages may have indistinct print especially if the original pages were typed with a poor typewriter ribbon or if the university sent us an inferior photocopy.

Reproduction in full or in part of this microform is governed by the Canadian Copyright Act, R.S.C. 1970, c. C-30, and subsequent amendments.

AVIS

La qualité de cette microforme dépend grandement de la qualité de la thèse soumise au microfilmage. Nous avons tout fait pour assurer une qualité supérieure de reproduction.

S'il manque des pages, veuillez communiquer avec l'université qui a conféré le grade.

La qualité d'impression de certaines pages peut laisser à désirer, surtout si les pages originales ont été dactylographiées à l'aide d'un ruban usé ou si l'université nous a fait parvenir une photocopie de qualité inférieure.

La reproduction, même partielle, de cette microforme est soumise à la Loi canadienne sur le droit d'auteur, SRC 1970, c. C-30, et ses amendements subséquents.

Canada

A Numerical Investigation of the Coastal Frontal Cyclogenesis of 3-4 October 1987

by

Jianjie Wang

A thesis submitted to the

Faculty of Graduate Studies and Research

in partial fulfilment of the requirements for the degree of

Master of Science

Department of Atmospheric and Oceanic Sciences

McGill University, Montreal, Quebec

CANADA

ISBN 0-612-12288-3

Canada

Résumé

La prévision réussite et la compréhension physique de la cyclogenèse côtière secondaire demeurent parmi les plus grands défis auxquels font face les scientifiques atmosphériques aujourd'hui. Dans cette étude, un événement de cyclogenèse rapide le long de la côte-est américaine ayant eu lieu le 3-4 octobre 1987 est étudié utilisant une version à grille pilotée du modèle mésoéchelle de Penn State/NCAR (MM4) avec une grille fine de 25km de résolution. Il est démontré que le modèle MM4 reproduit convenablement la croissance du cyclone s'étant formé dans une zone frontale côtière, son déplacement subséquent, son intensité, ses structures de circulation et la précipitation associée au système. On trouve que la cyclogenèse côtière se produit dans un environnement favorable à large échelle avec une advection thermique prononcée dans la basse troposphère et une forte concentration de tourbillon potentiel (TP) à haut niveau associé à la dépression de la tropopause. Le transport d'air chaud et humide de la couche limite maritime vers la côte par la circulation à basse niveau fournit l'énergie latente nécessaire pour la production de précipitation forte observée ainsi que pour une variété de phénomènes météorologiques.

Une série de simulations de sensibilité de 24 heures sont complétées afin d'examiner l'importance relative du réchauffement diabatique, des facteurs à la large échelle et de la qualité des conditions initiales dans la cyclogenèse. On trouve que la libération de chaleur latente est responsable de 28% du creusement total du cyclone. L'impact moins important de la chaleur latente peut être attribuée au développement de fortes précipitations dans le

secteur froid, de façon à ce que le TP induit par le réchauffement à tendance à être advecté rapidement hors du centre du cyclone. L'étude du budget du tourbillon démontre que l'advection thermique à bas niveau domine la genèse lors du développement initial, tandis que les facteurs à large échelle associés à la dépression de la tropopause déterminent le creusement rapide plus tard dans le développement ainsi que la pression centrale finale de la tempête. Afin de déterminer la raison pour laquelle les modèles numériques n'ont pu réussir à correctement prédire tous les scénarios observés, une expérience dynamique de "nudging" est faite pour produire un ensemble de données "vraies". Une comparaison de ce résultat avec d'autres études de sensibilité révèle que la sous-prévision de la pression centrale du système ainsi que d'autres caractéristiques de la circulation sont associées aux déficiences dans le couplage vertical du cyclone à la surface et à l'anomalie de TP à haut-niveau, qui est, en revanche, causé par les incertitudes dans la structure thermique au-dessus de l'océan à bas niveaux.

Abstract

The successful prediction and physical understanding of secondary, coastal cyclogenesis remain one of the most difficult challenges facing atmospheric scientists today. In this study, a rapidly east-coastal cyclogenesis event that took place during 3-4 October 1987 is investigated using a nested-grid version of the Penn State/NCAR mesoscale model (MM4) with a fine mesh grid size of 25 km. It is shown that the MM4 model reproduces reasonably well the growth of the cyclone from a coastal frontal zone, its subsequent track, intensity, circulation structures and its associated precipitation. It is found that the coastal cyclogenesis occurs in a favorable large-scale environment with pronounced thermal advection in the lower troposphere and marked potential vorticity (PV) concentration aloft associated with the tropopause depression. The transport of warm and moist air from the marine boundary layer by the low-level inshore flow provides the necessary latent energy for the production of the observed heavy precipitation and a variety of weather phenomena.

A series of 24-h sensitivity simulations are performed to examine the relative importance of diabatic heating, large-scale forcing and the quality of initial conditions in the cyclogenesis. It is found that latent heat release accounts for 28% of the total deepening of the cyclone. The less significant impact of the latent heating could be attributed to the development of heavy precipitation in the cold sector such that the heating-induced PV tends to be quickly advected away from the cyclone center. Vorticity budget diagnosis shows that the low-level thermal advection dominates the genesis during the incipient stages, whereas

the upper-level forcing associated with the tropopause depression determines the rapid deepening rate at later stages and the final depth of the storm. To determine why several model simulations failed in predicting correctly all of the observed scenarios, a dynamical nudging experiment is conducted to provide a "ground-truth" dataset. A comparison of this simulation result with other sensitivity simulations reveal that the underprediction of the system's central pressure and other circulation features is closely related to the poor vertical coupling between the surface cyclone and upper-level PV anomaly, which in turn is caused by the initial uncertainties in the low-level thermal structure over the ocean.

Table of Contents

List of Figures

List of Tables

Acknowledgements

First and foremost, I sincerely thank my supervisor, Professor Da-Lin Zhang, for his expert supervision and kind encouragement throughout this thesis work. I benefited greatly from his deep knowledge in mesoscale and large-scale modelling, dynamics and physics, and from his dedication to scientific work. I acknowledge that the computations for this work were performed on CRAY-YMP of the National Centre for Atmospheric Research, which is sponsored by the National Science Foundation.

I especially thank Mr. Ning Bao for his timely assistance in running the PSU/NCAR mesoscale modelling system. I also thank my colleagues, Mr. Rick Danielson and Mr. Zonghui Huo for their helpful discussions and friendly presence, as well as my friends in the department for their humour and friendship during the research. Dr. Garry Lackmann is acknowledged for his assistance in obtaining the ω-equation solver for the present study, and Mr. Dov Bensimon for translating the abstract of this thesis in French.

I wish to express my gratitude to my parents. Without their constant moral support and encouragement this work would not have been possible.

Finally, very special thanks go to my husband, Guoguang, for his love and understanding over the past two years, and to my son, Han, for his very important moral support which only children can offer.

Chapter 1 Introduction

1.1 East coastal cyclogenesis

The east coastal region of North America has been noted as one of the most active cyclogenetic regions of the world (Petterssen 1941, 1956; Hayden 1981; Whittaker and Horn 1981; Kocin and Uccellini 1990). Cyclones also tend to undergo explosive deepening once they move offshore (Sanders and Gyakum 1980). From a theoretical viewpoint, the essential mechanisms governing extratropical atmospheric motion are well understood in terms of Rossby wave propagation and baroclinic instability. However, there are many physical processes, such as orography, latent heating, surface fluxes of heat, moisture and momentum, and the land-ocean interface, involved in the coastal cyclogenesis, that make this type of studies more complicated and attractive.

It has been noticed by previous observational and numerical studies that the coastal frontal zone is often a site for cyclogenesis (Bosart 1975; Bosart 1981; Bosart and Lin 1984; Uccellini et al. 1987; Stauffer and Warner 1987; Doyle and Warner 1990), in which cyclone is initiated as an incipient wave usually with an along-front wavelength of 1000-2000 km. The phenomenon of disturbances developing within a localized baroclinic zone resembles polar front cyclogenesis. As an accepted conceptual model of frontal cyclogenesis, the classic polar front theory (Bjerknes 1919; Bjerknes and Solberg 1922) attributes the occurrence of the waves to an instability of the frontal surface and views the development of cyclones as the growth to finite amplitude of the frontal waves. It has been noticed by

Charney (1975) and others (Harrold and Browning 1969; Nitta and Ogura 1972; Reed 1979) that there is a problem in reconciling the relatively short length scale of frontal wave with conventional baroclinic instability theory which shows disturbances with scale of 3000-4000 km to be the most unstable (Simmons and Hoskins 1976). Therefore, many theoretical researches have been based upon attempts to complement classical baroclinic instability theory. Some relevant works are Killworth (1980), Moore and Peltier (1987), Schär and Davies (1990) and Joly and Thorpe (1990). Moore and Peltier (1987) found an unstable wave mode that grew mainly by baroclinic energy conversion using a primitive equation system. Joly and Thorpe (1990) added a low-level maximum of potential vorticity generated by latent heat release into the properties of unstable waves, and their modes obtained significant energy from the kinetic energy of the basic state. Schär and Davies (1990) showed that the source and nature of the instability is a vortex interaction effect acting across the thermal maximum of the warm band based upon a quasi- and semi-geostrophic framework. It seems that the mechanisms of frontal cyclogenesis can be categorized as two, in situ instability (i.e., localized instability in the lower level and/or boundary) and upper-lower level interaction. The advection of a deep upper-level trough toward a trailing front is able to act as the initial disturbance for a potential frontal instability, whereas an appropriate frontal wave development could institute a horizontal spatial scale and a favoured location for the upper- and low-level baroclinic interaction.

Numerous observational and numerical studies have also been carried out for east coastal cyclogenesis and related phenomena [e.g., coastal frontogenesis, cold-air damming, low-level jet (LLJ), and etc.]. Sanders (1986, 1987) studied the structure, the mean

behaviour of coastal cyclones, and the correlations of the east coastal cyclogenesis with the upper-level forcing (500 hPa vorticity maxima) and the baroclinic forcing from a composite approach. He showed that the upper-level forcing is a necessary but far from a sufficient condition for explosive cyclogenesis, and the intensity of the baroclinic forcing influences the probability of explosive response. It has been revealed that the LLJ is important in many ways to enhance coastal cyclogenesis (Uccellini et al. 1987; Sjostedt et al. 1990; Doyle and Warner 1991). Chen et al. (1983), and Anthes et al. (1983) found notable influences on the phase speed and the intensity of a coastal storm and on the vertical coupling between upper- and low-level processes due to latent heating based on numerical studies, while Lapenta and Seaman (1992) showed a case in which without latent heating, cyclogenesis does not occur along the Carolina coastal front despite the presence of strong low-level baroclinicity and cyclonic vorticity. Doyle and Warner (1992) documented a coastal frontal cyclogenesis case supporting similar idea that the strong low-level diabatic forcing is essential. There are also some studies focusing on dynamic and thermodynamic structures of eastern coastal cyclones (Uccellini et al. 1984, 1985; Uccellini and Kocin 1987; Lapenta and Seaman 1990). Extensive studies on east coastal cyclogenesis are leading to the recognition that the individual process may be necessary for the development of cyclones but is not sufficient when acting alone to produce rapid cyclogenesis. The nonlinear interaction among the various dynamic and thermodynamic processes within relatively small space and temporal domains is crucial for the rapid evolution of these storms.

In spite of the effort that has been brought to bear on the east coastal cyclogenesis, the ability to forecast the genesis and evolution of these storms is still limited. The earlier

operational models experienced difficulties in predicting this type of storms (Leary 1971; Sanders 1987; Bosart and Sanders 1991). This is a consequence of the lack of detailed knowledge as to the processes responsible for their existence and to their pronounced case-to-case variability, especially those growing from the coastal frontal zone as mesoscale perturbations. Therefore, case studies on coastal cyclogenesis events are necessary for providing evidence to theoretical descriptions, for investigating the nature of coastal cyclogenesis, and for better understanding the interaction of different processes leading to coastal cyclogenesis, thus in hopes of improving the ability of numerical weather prediction.

1.2 Objectives of the thesis

The purpose of this thesis is to study a frontal cyclogenesis event, that underwent a nearly explosive development and dropped heavy snow and rainfall over eastern New York and western New England during 3-4 October 1987, using the Pennsylvania State University/National Center for Atmospheric Research (PSU/NCAR) Mesoscale Model (MM4; Anthes and Warner 1978; Anthes et al. 1987). This case is selected for this study, not only because it was one of those predicted poorly by the then operational models but also because this was an unprecedented early-season snowstorm over the coastal region in accordance to Bosart and Sanders (1991), hereafter referred to as BS91. BS91 have documented the evolution of this storm using conventional surface and upper-air observations, and analyzed the performance of the operational guidance from the National Meteorological Center (NMC) Regional Analysis and Forecast System (RAFS) for this event. Their study suggests that i) the storm life cycle follows well-known qualitative quasi-geostrophic development principle;

ii) the cooling by melting snow is a crucial factor in allowing snow to reach the surface; and iii) poor initial conditions over the middle Atlantic coast region, namely, underestimations of the low-level vorticity and convergence in the coastal baroclinic zone and the mean relative humidities in the lower troposphere, are responsible for the failure of the operational models in predicting this storm event. There are several questions remaining unanswered. For example, what are the relative contributions of dynamic versus thermodynamic forcings and latent heat release to the coastal cyclogenesis? To what extent is the quasi-geostrophic development theory responsible for the rapid deepening? Why did the then operational models fail to predict the cyclogenesis from the coastal frontal zone if the storm follows quasi-geostrophic theory? How sensitive is the model prediction to the initial uncertainties over the coastal region? What was the mechanism by which the observed heavy precipitation was generated and where was the source of moisture? The difficulty of obtaining high quality data, particularly in the offshore area, poses some serious limitations to the BS91 analysis as well as to the understanding of the structures and evolution of the coastal cyclone. Therefore, in this study we attempt to address the above issues and provide some insight into the physical processes leading to the cyclogenesis through a number of numerical simulations using the MM4. A 24-h simulation (i.e., from 1200 UTC 3 to 1200 UTC 4 October 1987) will be used to investigate the cyclogenesis processes, which covers just the cyclone development from its incipient to mature stages.

The objectives of this thesis are to:

i) replicate reasonably the genesis and rapid deepening of the coastal cyclone as well as its associated precipitation during the 24-h period, as verified against the BS91 analysis

and other available observations;

ii) evaluate the sensitivity of the model-simulated cyclogenesis to latent heat release, different initial conditions and other model physical representations;

iii) quantify the different physical processes taking place in the frontal cyclogenesis and clarify the relative importance of upper- and low-level forcings in the genesis during the different stages of the cyclonic development;

iv) examine BS91's hypothesis on the quasi-geostrophic nature of the cyclogenesis event, and determine the numerical predictability of the storm; and

v) clarify the mechanism(s) whereby the observed heavy precipitation was generated and examine the source of moisture into the region.

The organization of the thesis is given as follows. Chapter 2 describes the model features and the initial conditions for the present study. Chapter 3 provides synoptic description of the sequence of the frontal cyclogenesis and verification of the 24-h model simulation. Chapter 4 examines the sensitivity of the model simulation to latent heat release and different initial conditions. The relative importance of upper- and low-level forcing to the cyclogenesis, and the numerical predictability of the storm will also be discussed. A summary and concluding remarks are given in the final chapter.

Chapter 2 Model Description and Initial Conditions

An improved version of the PSU/NCAR mesoscale model (MM4) is used for the present study (Anthes and Warner 1978; Anthes et al. 1987). The MM4 model is a three-dimensional, hydrostatic, primitive equation model with four-dimensional data assimilation (FDDA) capabilities. Sections 2.1 — 2.3 provide brief descriptions of the respective model dynamics, physical representations and the dynamics nudging technique used in the MM4 modelling system. Table 2.1 lists the basic features of the MM4 model used for the present study.

2.1 Model dynamics

The governing equations used in the MM4 model are formulated in terrain-following sigma (σ) coordinates,

$$\sigma = \frac{p - p_t}{p^*} \quad , \qquad (2.1)$$

where p is pressure, p_t is the pressure at the top of the model (in the present case 70 hPa); $p^* = p_s - p_t$; and p_s is the surface pressure. The model equations are written in flux form, where prognostic variables for horizontal winds, temperature, mixing ratio, cloud water (ice), and rain water (snow) are mass weighted by p^* (i.e., p^*u, p^*v, p^*T, p^*q_v, p^*q_c and p^*q_r).

The present version of the MM4 contains a two-way interactive nested-grid procedure (Zhang et al. 1986), in which the coarse-grid mesh (CGM) uses an array of 49 × 59 grid

Table 2.1 Summary of the dynamics and physics of the MM4 model

Dynamics
★ Hydrostatic primitive equations, u, v, T, q and p_s predictive (Anthes et al. 1987)
★ Two-way interactive nested-grid procedure (Zhang et al. 1986)
★ Time-dependent lateral boundary conditions for the CGM, based on conventional observations
★ Brown and Campana (1978) time discretization
★ Staggered horizontal grid overlaid on a Lambert conformal map projection (25 km grid length for the FGM and 75 km for the CGM)
★ 19 staggered σ-levels (normalized pressure) with top at p_t = 70 hPa
★ Time step of 40 s for the FGM and 120 s for the CGM
★ Fourth-order horizontal diffusion
Physics
★ The Kain-Fritsch (1990, 1993) convective parameterization scheme for the FGM
★ The Anthes H. L./Kuo type convective parameterization for the CGM (Anthes et al. 1987)
★ Explicit moisture scheme with predictive equations for cloud water (ice) and rain water (snow) and bulk treatment of the microphysics (Hsie et al. 1984; Zhang 1989)
★ Modified Blackadar (1979) PBL treatment (Zhang and Anthes 1982)
★ Surface fluxes computed from similarity theory
★ Implicit vertical diffusion
★ Prediction of ground temperature following the "force-restore" slab model

points, spaced 75 km apart, and the fine-grid mesh (FGM) has an array of 73 × 91 grid points with a grid size of 25 km (see Fig. 2.1). There is no nesting in the vertical; so both the CGM and FGM have 20 σ-levels (i.e., 0.0, 0.05, 0.1, 0.15, 0.206, 0.263, 0.321, 0.38, 0.44, 0.501, 0.562, 0.619, 0.676, 0.733, 0.789, 0.845, 0.901, 0.957, 0.99, 1.0), which gives 19 layers of unequal thickness. The nesting procedure is designed to improve the horizontal resolution in model forecasts of small-scale atmospheric phenomena, and better resolve large gradients of meteorological variables without requiring a FGM throughout the entire model domain. The nesting procedure also permits the successful incorporation of realistic complex terrain into the model.

Both the CGM and FGM are staggered in the horizontal and vertical. In the horizontal staggering, momentum variables are defined at "dot" points while all the other variables are defined at "cross" points (Fig. 2.2), i.e., the Arakawa-B grid (Arakawa and Lamb 1977). In the vertical staggering, the vertical velocity in σ-coordinates, ($\dot{\sigma}$), is computed on full σ-levels while all the other variables are defined on half σ-levels. The size of the FGM domain is chosen such that the storm's circulations being simulated could be covered during the 24-h integration period, whereas the outmost lateral boundaries of the CGM are located far enough away from the region of interest so that the errors introduced at the boundaries remain within some acceptable tolerance in the interior of the domain. The lateral boundary conditions for the CGM are specified from observations by temporally interpolating the 12-hourly enhanced analyses according to Perkey and Kreitzberg (1976). The lateral boundary conditions for the FGM are updated every time step by interpolating all CGM's flux tendencies along the mesh interfaces.

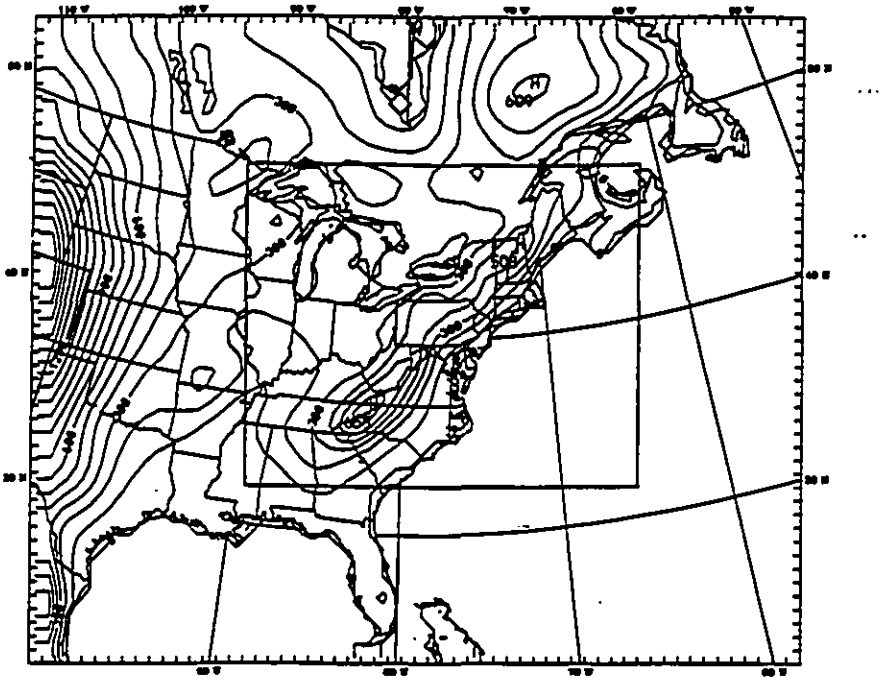

Fig. 2.1 Distribution of topography at intervals of 100 m over the model nested-domain. Interior box indicates the fine-mesh portion of the domain. The intervals marked on the frame are mesh grids (75 km for coarse mesh and 25 km for fine mesh).

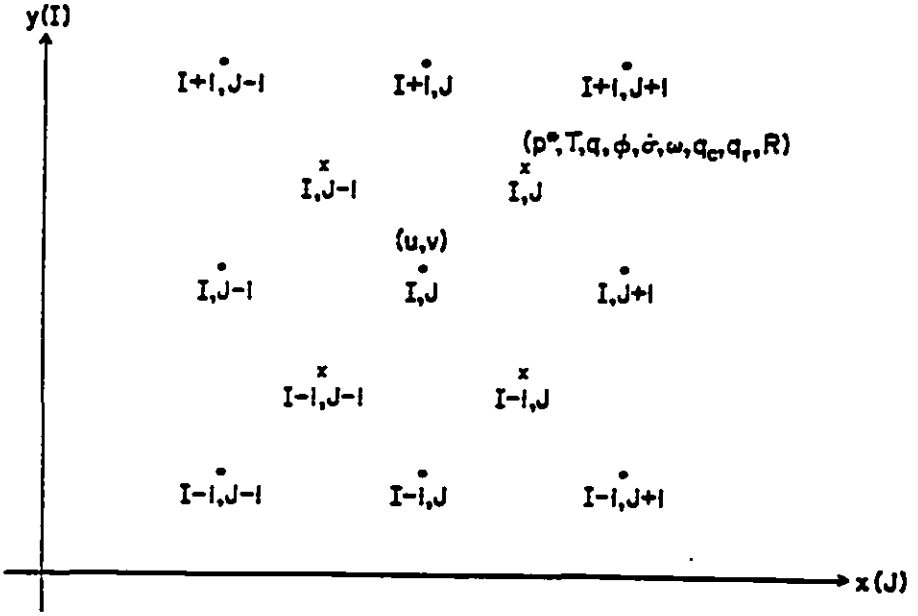

Fig. 2.2 Schematic horizontal grid structure of the PSU/NCAR model, taken from Anthes et al. (1987).

The MM4 model uses the Brown and Campana (1978) time-integration scheme, which allows for a time step approximately 1.6 times larger than that allowed by the conventional leapfrog scheme and produces virtually identical results. In the present study, time steps of 40 and 120 seconds are used for the CGM and FGM, respectively.

2.2 Model physics

a. Explicit and implicit convective schemes

The treatment of convective processes in large-scale and mesoscale models as the grid size decreases is a fundamental problem in numerical weather prediction. On the one hand, a reasonable explicit scheme is necessary when the grid size is small enough to resolve meso-β scale circulations and associated phase changes. On the other hand, an appropriate convective parameterization scheme is needed to represent the effects of subgrid-scale updrafts, downdrafts and compensating subsidence. Thus, an explicit moisture scheme and an implicit convective scheme should be simultaneously used to account for the separate effects of mesoscale (resolvable-scale) and subgrid-scale convection, the so-called "hybrid approach" (Zhang et al. 1988; Molinari and Dudek 1992; Zhang et al. 1994). As discussed by Zhang et al. (1988), the simultaneous incorporation of implicit and explicit convective schemes does not double account for either resolvable-scale or subgrid-scale heating and moistening since explicit schemes neglect subgrid eddy fluxes that implicit schemes handle. Previous studies have shown that the "hybrid method" appears to be the best approach to handling convective and stratiform (resolvable-scale) precipitation in nature (e.g., Zhang et al. 1988).

In this study, an explicit scheme containing prognostic equations of cloud water (ice) and rainwater (snow) (Hsie et al. 1984; Zhang 1989; Dudhia 1989) is coupled with the implicit convective schemes of the Kain-Fritsch (1990, 1993) for the FGM and the Anthes H. L./Kuo (Anthes et al. 1987) for the CGM. The explicit moisture scheme contains the effects of virtual temperature, hydrostatic water loading, condensation and evaporation, freezing and melting, and depositional and sublimation processes. The Kain-Fritsch convective scheme uses a cloud model that includes the effects of updrafts, moist downdrafts and compensating subsidence. The scheme also allows updraft entrainment and detrainment rates to vary more realistically as a function of environmental conditions, and permits the direct feedback of both vapor and hydrometeor to the grid scale, thereby eliminating the uncertainty associated with the sedimentation process in the Fritsch-Chappell scheme (see Zhang et al. 1994).

b. Planetary boundary layer scheme

The Blackadar high-resolution planetary boundary layer (PBL) scheme is used to represent vertical exchanges between the free atmosphere and the underlying boundary layer (see Zhang and Anthes 1982; Zhang and Fritsch 1986).

The scheme consists of two modules to predict the time-dependent behaviour of the PBL under various surface characteristics. Under stable conditions, turbulent fluxes are related to a local Richardson number. In contrast, under conditions of free convection, the exchange of heat, moisture and momentum occurs through mixing between convective elements originating at the surface and environmental air in the PBL. The surface temperature, T_g, over land is computed from a surface energy budget based on a "force-restore" slab model developed by Blackadar (1976, 1979), which is given by

$$C_g \frac{\delta T_g}{\delta T} = R_n - H_m - H_s - L_v E_s + C_g \frac{\partial \theta_g}{\partial t}\Big|_{conv} , \qquad (2.2)$$

where C_g is the thermal capacity of the slab per unit area (J m^{-2} K^{-1}); R_n denotes the net radiation; H_m is the heat flow into the substrate; H_s represents the sensible heat flux into the atmosphere; L_v denotes the latent heat of vaporization; E_s is the surface moisture flux; and $\partial\theta_g/\partial t|_{conv}$ is the ground potential temperature tendency due to deep convection taken as the tendency produced by the Kain-Fritsch scheme for the first model layer. The net radiation, R_n, accounts for the effects of water vapor absorption, clouds, multiple backscattering and reflection from aerosols as well as for cloud and precipitable water influences on downward infrared radiative flux. The heat flow into the ground, H_m, is calculated through a simple first-order diffusion process with the soil temperature being specified and kept fixed throughout the period of the integration. Finally, the sensible and moisture fluxes into the atmosphere are computed from similarity theory. All the basic parameters required for the surface budget calculations, i.e., moisture availability, surface albedo, roughness length, thermal capacity and surface emissivity, are derived from the land-use data archived at NCAR and given by a look-up table which assigns one value of a surface index for each grid point of the domain.

Over water surfaces, the surface temperature is assumed to be constant rather than predicted from Eq. (2.2). The heat and moisture fluxes are also computed from similarity theory, but with roughness length given by

$$Z_0 = Z_{0b} + 0.032\ u_*^2 / g , \qquad (2.3)$$

where z_{0b} is a background roughness length of 10^{-4} m, u_* denotes the frictional velocity and g is gravity (Delsol et al. 1971).

2.3 Nudging technique

To generate high-quality four-dimensional mesoscale analyses for diagnostic purposes, the Newtonian relaxation (or nudging) developed by Stauffer and Seaman (1990) is utilized for the present study. This FDDA technique is a continuous assimilation method that relaxes the model state toward the observed state by adding to one or more of the prognostic equations artificial tendency terms based on the difference between the two states. The model solution could be nudged toward either gridded analyses or individual observations during a period of time surrounding the observation (Stauffer and Seaman 1990; Stauffer et al. 1991).

Nudging to an analysis is used in this study. As discussed in Stauffer and Seaman (1990), when pressure is not assimilated, the general form of the predictive equation for variable $\alpha(\mathbf{X}, t)$ is written in flux form as

$$\frac{\partial p^* \alpha}{\partial t} = F(\alpha, \boldsymbol{X}, t) + G_\alpha \cdot W_\alpha(\boldsymbol{X}, t) \cdot \epsilon_\alpha(\boldsymbol{X}) \cdot p^* \cdot (\alpha_0 - \alpha) \ , \qquad (2.4)$$

where F denotes all of the model's physical forcing terms (advection, Coriolis, etc.); α represents any model-prognostic variable; α_0 is the corresponding analysis; $\mathbf{X}$ are the independent spatial variables; t is time; G_α denotes the nudging factor; and W_α is weighting function ($W_\alpha = W_{xy} \cdot W_\sigma \cdot W_t$), which determines spatial and temporal variation of the nudging term. The analysis confidence factor, ε_α, ranges between 0 and 1 based on the quality and distribution of the data that went into the analysis.

Typical values of G_α are $10^{-4} - 10^{-3}$ s^{-1} for meteorological systems. Too large G_α will force the model state over strongly toward the observations, since the abilities of the model to generate its own mesoscale structures and to resolve mass-momentum imbalances will

decrease by heavy insertion of the observed analyses. On the other hand, too small G_α is undesirable because the observations will have minimal impact on the evolution of the model state. Hence, in the present study, $G_\alpha = 3 \times 10^{-4}$ is chosen (Stauffer et al. 1985), which satisfies the numerical stability criterion, $G_\alpha \leq 1/\Delta t$. With the adequate value of G_α, the nudging technique not only limits the large scale model errors, such as phase and amplitude errors, to grow with time, but also provides coherence and dynamic balance among the different meteorological fields, thus producing the best possible numerical representation of the atmosphere with mesoscale circulation structures. A dataset with time continuity and dynamic coupling among the fields will be generated for dynamic analysis of the case.

2.4 Model initialization and initial conditions

Accurate specification of the initial mass and wind fields is crucial for obtaining a high quality forecast. In the present study, the initial conditions were obtained by first interpolating the NMC operational global analysis to the mesoscale model grid points as the first guess, and then enhancing it with all available rawinsonde observations at mandatory and significant levels using the Cressman-type of successive correction scheme (Benjamin and Seaman 1985). No subjectively prepared soundings were used, except over the ocean where the thermal perturbation in the BS91 surface analysis has been included, to a certain extent, in the lowest 150 hPa. As will be shown in section 4.2, this is a necessary step to obtain a meaningful improvement of the initial conditions, since the model tends to "forget" the surface observations rather quickly if they are only incorporated into a shallow layer. The sea surface temperature was derived from the NMC global analysis without further enhancement, but the

ship reports and buoy data were used to enhance the analysis of surface temperature, humidity, and wind fields. No balancing between the mass and wind fields was done. However, the vertically integrated divergence was set to zero in order to minimize gravity wave noise in the first few hours of integration.

The model was initialized at 1200 UTC 3 October 1987, which was prior to the development of the coastal cyclone. Figs. 2.3 and 2.4a-c show the model initial conditions at the surface and 300, 500, and 850 hPa over the CGM, respectively. The principal features of interest at the surface include i) a coastal trough that extends from the primary low-pressure system over southern Quebec into eastern North Carolina; and ii) a shallow oceanic mesolow to the east of North Carolina that originated from lower latitudes (Fig. 2.3). There were a significant wind shift and a modest baroclinic zone across the coastal trough, with an intense pressure gradient in the cold air. These baroclinic structures tilted westward, except for the primary low, up to 700 hPa where a changeover to equivalent barotropic conditions occurred. For example, at 850 hPa, there was a significant phase lag between the thermal and height troughs (Fig. 2.4c), indicating cold (warm) advection behind (ahead of) the coastal trough. The coastal cyclone was about to develop roughly off the coast of New Jersey (BS91).

Higher up, there was an intense large-scale though in the upper half portion of the troposphere, with maximum absolute vorticity or potential vorticity (PV) located at the base (i.e., over eastern Kentucky, see Figs. 2.4a, b). Thus, positive vorticity advection by southwesterly winds spread along the middle Atlantic coast. However, the trough was in phase with a thermal wave so that its cold core coincided with the trough axis, which suggests equivalent barotropical conditions aloft and little contribution of upper-level thermal advection

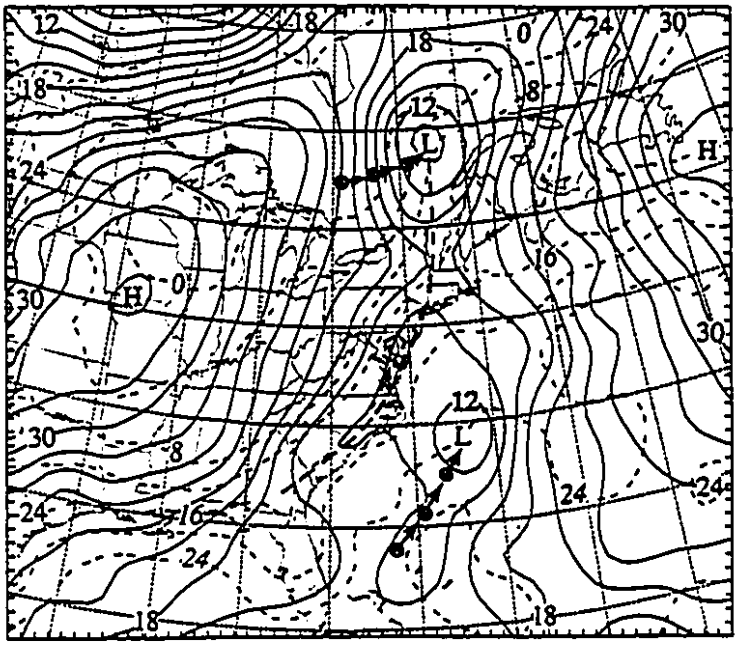

Fig. 2.3 Sea-level pressure (solid) at intervals of 2 hPa and temperature (dashed) at intervals of 4 °C at the model initial time (i.e., 1200 UTC 3 October 1987). The mark " ⊗→⊗→ " denotes the previous paths of the low systems; the thick dashed line represents subjectively analyzed trough.

a)

b)

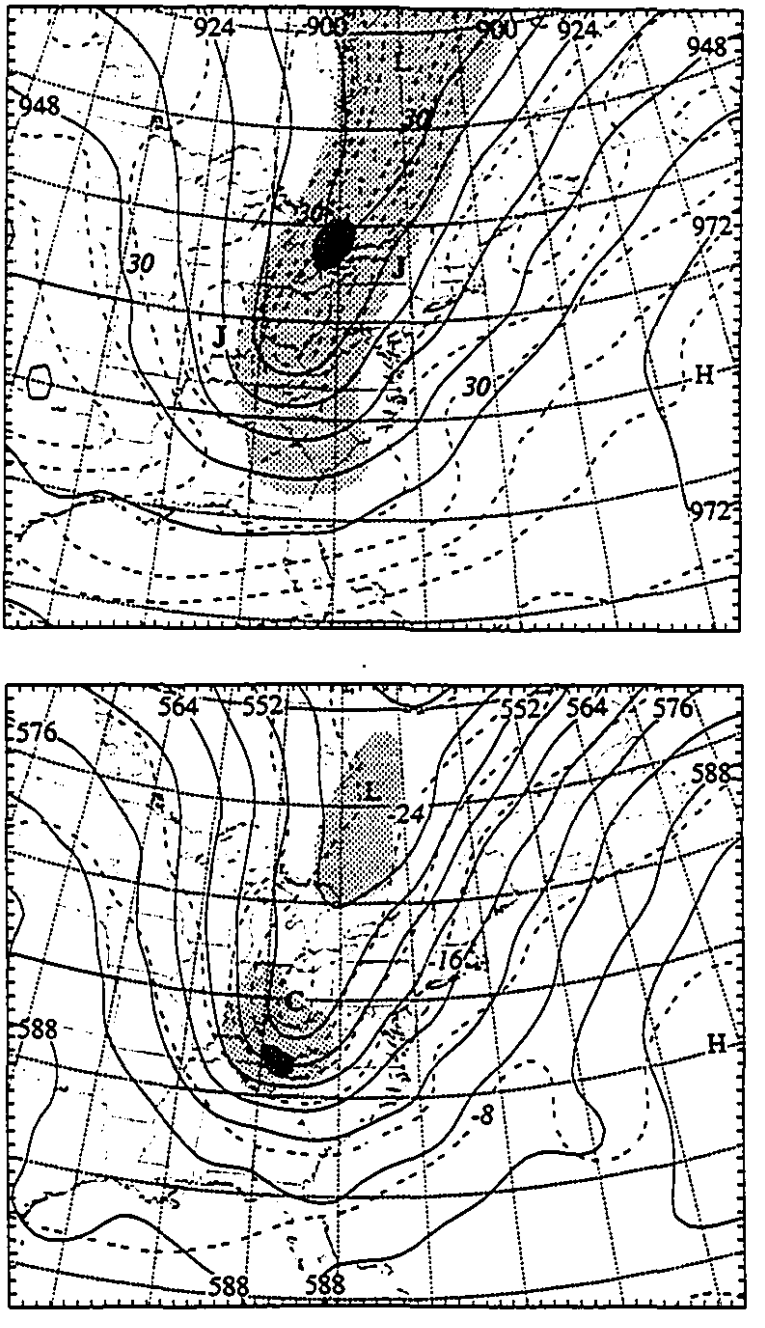

Fig. 2.4 Enhanced NMC analysis at the model initial time (i.e., 1200 UTC 3 October 1987): (a) 300 hPa height (solid) at intervals of 12 dam and isotach (dashed) at intervals of 10 m s^{-1}, superposed with PV > 2 PVUs (lightly shaded) and > 8 PVUs (heavily shaded); (b) 500 hPa height (solid) at intervals of 6 dam and isotherm (dashed) at intervals of 4 °C, superposed with absolute vorticity > 2×10^{-4} s^{-1} (lightly shaded) and > 3×10^{-4} s^{-1} (heavily shaded); (c) 850 hPa height at intervals of 3 dam and isotherm at intervals of 4 °C, superposed with PV > 1 PVU (lightly shaded) and > 2 PVUs (heavily shaded).

c)

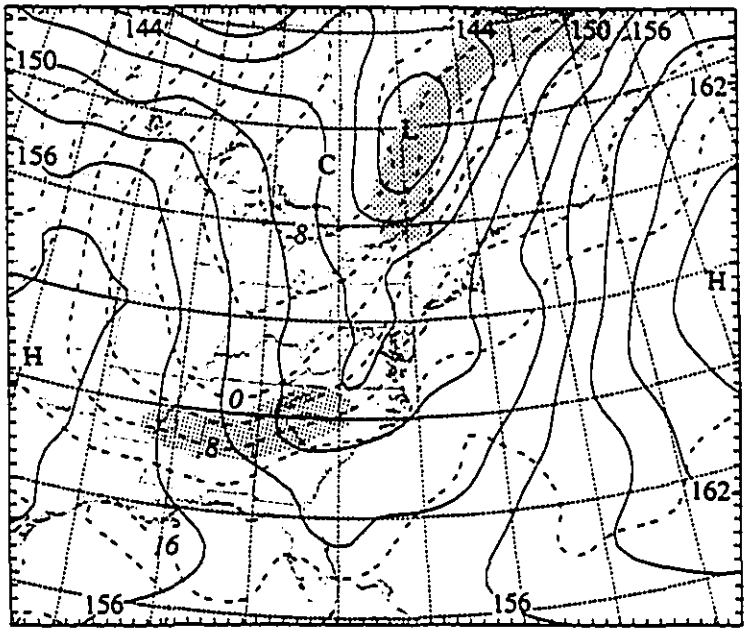

Fig. 2.4 (*Continued*)

to the subsequent cyclogenesis. Associated with the upper-level trough was an intense jet stream, extending from central Canada through the Great Lakes to Tennessee and then turning northeastward along the east coast (Fig. 2.4a), with the double-core structure like that discussed by Thorpe (1985). The general increase of the southwesterly flow ahead of the trough axis implies the presence of upper-level divergence over the east coastal region. Furthermore, the PV distribution showed the downward extrusion of the stratospheric air along the trough axis, if a typical value of 2 PVUs (1 PVU = 10^{-6} m^2 K s^{-1} kg^{-1}) is used to define the dynamical tropopause.

It should be mentioned that because the present cyclogenesis occurred offshore where no upper-air observations were available for enhancing the NMC analysis, the uncertainties in the model initial conditions would certainly affect the predictability of the coastal cyclogenesis. In particular, most of the air mass in the warm sector entered the associated cyclonic circulations from the data-void ocean. Furthermore, the oceanic mesolow, which moved northeastward and eventually merged into the coastal cyclone (see BS91), could not be realistically represented in the initial conditions due to the lack of upper-air data.

Chapter 3 Case Description and Model Performance

In this chapter, we document the sequence of the coastal cyclogenesis event from its incipient to mature stages (i.e., from 1200 UTC 3 to 1200 UTC 4 October) using the objectively analyzed surface maps by BS91 and the GOES satellite imagery as well as our model simulations. Meanwhile, we verify the 24-h model simulation against the BS91 analysis and other available data. Since numerical models can often reproduce very well the intensity and evolution of large-scale flows, like the upper-level trough and jet streaks in the present case, we will focus primarily on the verification of the simulated surface features including the track and intensity of the coastal cyclone as well as its associated precipitation. The upper-level features of the system will be examined to help gain insight into the vertical structure and the processes leading to the cyclogenesis.

3.1 Development of the frontal cyclone

Figs. 3.1 and 3.2 compare the time series of the cyclone's tracks and central pressures between the MM4 simulation, the BS91 analysis and the then NMC's RAFS nested grid model (NGM) forecast. It is evident that the MM4-simulated cyclone follows the observed track reasonably well, including the cyclonic curvature during the first 12-h integration. In sharp contrast to our simulation, the NGM-predicted track is 270 km too far to the east of the observed at 1200 UTC 4 October (henceforth 4/12-24), needless to say the initial cyclone's curvature. More unfortunately, the NGM-predicted cyclone was intensified from

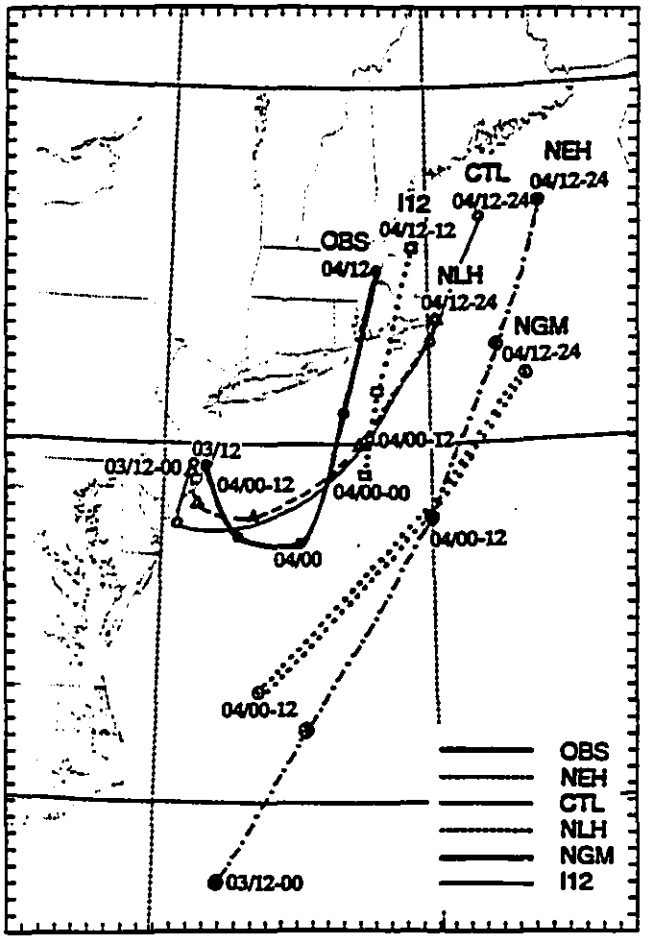

Fig. 3.1 Time traces of the coastal cyclone track from the BS91 analysis (thick solid), and Exps. NEH (no enhancement, dash-dotted), CTL (control, solid), NLH (no latent heating, dashed), NGM (NMC model, double dotted from BS91), and I12 (later initialization, dotted).

a wrong low-pressure system, i.e., the oceanic mesolow, rather than from a frontal disturbance (cf. Figs. 2.3 and 3.1). A similar scenario also appeared in a rapid continental mesoscale cyclogenesis event which occurred during 28-29 March 1984 (Kuo et al. 1995; Gyakum et al. 1995). To help understand why this happened, a sensitivity experiment was performed, in which the NMC analysis at 3/12-00 was interpolated to the present high-resolution grid mesh directly as the MM4's input (Exp. NEH). With the initial conditions, the MM4 produces a cyclone's track that is similar to the NGM-predicted (see Fig. 3.1), again resulting from the deepening of the oceanic mesolow. It is found that this scenario occurs because the signal of the oceanic mesolow, i.e., its associated cyclonic circulation, is much stronger than the coastal counterpart at its very genesis stage. It eventually develops into an intense coastal cyclone because it happens to propagate in a large-scale environment similar to the observed. It follows that incorporating as much information as possible (e.g., relatively higher-resolution observations in the vicinity of the genesis region, significant-level data and surface observations) into the model initial conditions could be critical in obtaining more realistic predictions of coastal or oceanic cyclones, particularly when their initial disturbances are very weak at the time of model initialization. This point has also been stressed by BS91 in their discussion on the failure of the NMC's operational forecast.

It is also evident that the model predicts fairly well the deepening of the coastal cyclone during the early genesis stages (Fig. 3.2). The difference in central pressure in the first 12-h integration is only about 1 hPa weaker than the NMC analysis and 3 hPa weaker than the BS91 analysis. However, this difference increases to 5 and 7 hPa, respectively, from the NMC and BS91 analyses at the end of the 24-h integration. During the second 12-h

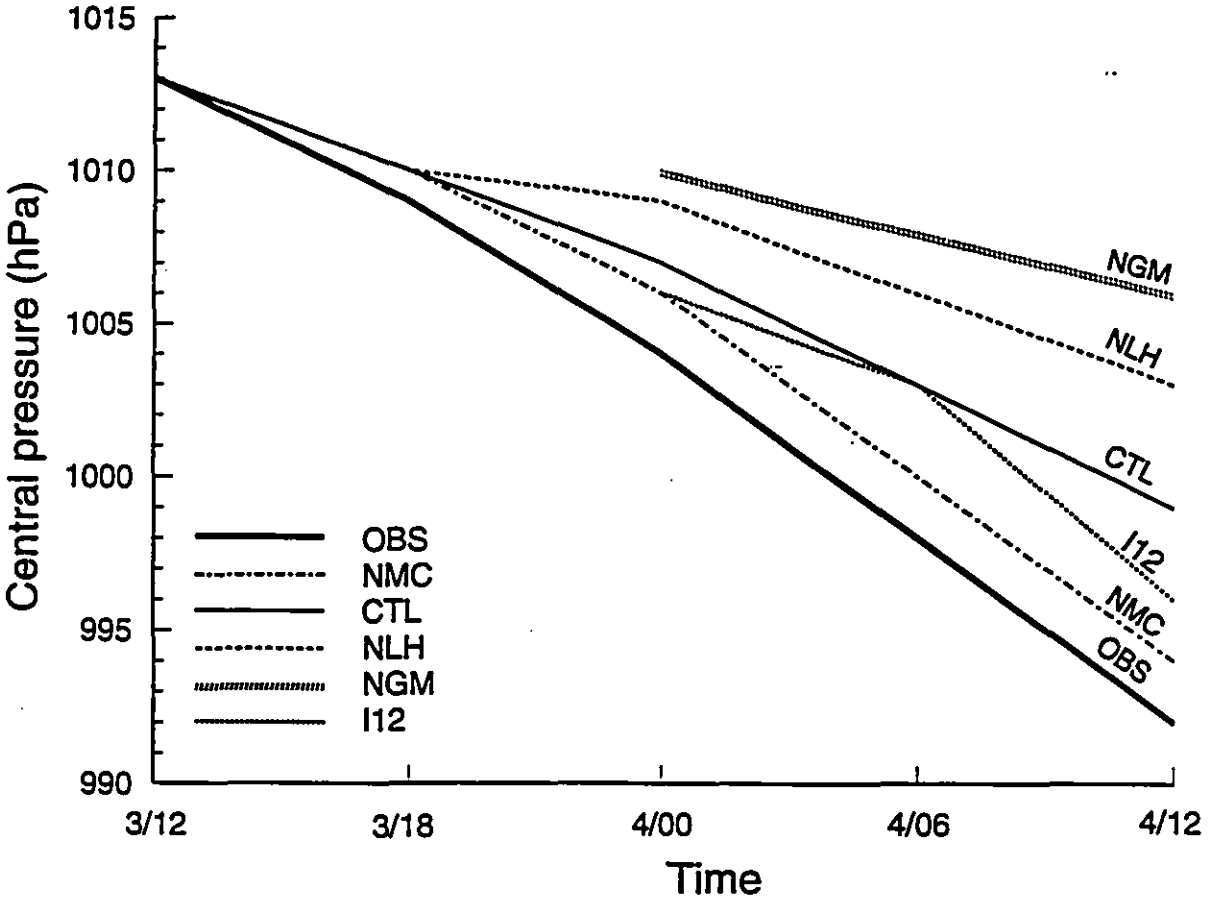

Fig. 3.2 Time series of the central mean-sea-level pressure of the coastal cyclone from the BS91 analysis (thick solid), the NMC analysis (dash-dotted), and Exps. CTL (control, solid), NLH (no latent heating, dashed), NGM (NMC model, double dotted), and I12 (later initialization, dotted).

period, the coastal cyclone intensified rapidly with a deepening rate of 1 hPa h^{-1}, whereas the model only captures 2/3 of the deepening. Nevertheless, the simulated cyclone also experiences a more rapid deepening (8 hPa) in the second than the first 12-h (6 hPa) period. By comparison, the NGM only predicted a 4-hPa deepening in the second 12-h period, i.e., about 1/3 of the observed rate. As will be discussed in section 4.2, the underprediction by both models can be attributed to the lack of proper vertical coupling between the surface low and the upper-level PV anomaly when they are too far apart.

Now let us examine how well the MM4 simulates the development of the coastal cyclone from a frontal disturbance and its subsequent mesoscale structures. As shown in Fig. 2.3, initially there were a parent cyclone located over central Quebec with a cold frontal trough extending southward along the east coast, and a weak oceanic mesolow (with a central pressure of 1010 hPa) of tropical origin to the east of North Carolina. Associated with them were two separate cloud systems: one was dominated by weak stratiform cloudiness in the cold sector of the continental cyclone, and the other by extensive deep clouds with considerable convective activity over the ocean (see Fig. 3.3a). Six hours later (i.e., at 3/18-06), the BS91 analysis shows that a low-pressure center off the New Jersey coast emerged from the front zone as it moved offshore (Fig. 3.4a). This implies that the coastal cyclone under investigation was spawned in a polar frontal zone, and thus it could be indeed regarded as a frontal cyclone. As the cyclogenesis began, a wider area of precipitation occurred in the cold sector.

Encouragingly, the MM4 model reproduces the development of a low-pressure center at nearly the right place in the frontal zone. The general distribution of precipitation behind

a)

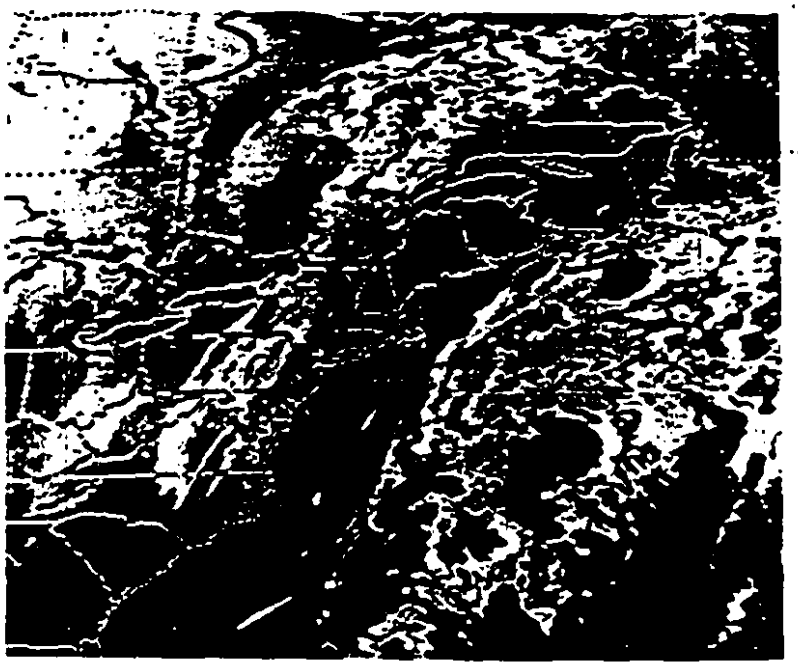

b)

Fig. 3.3 Enhanced infrared satellite imagery at (a) 1200 UTC 3; (b) 0000 UTC 4; and (c) 1200 UTC 4 October 1987.

c)

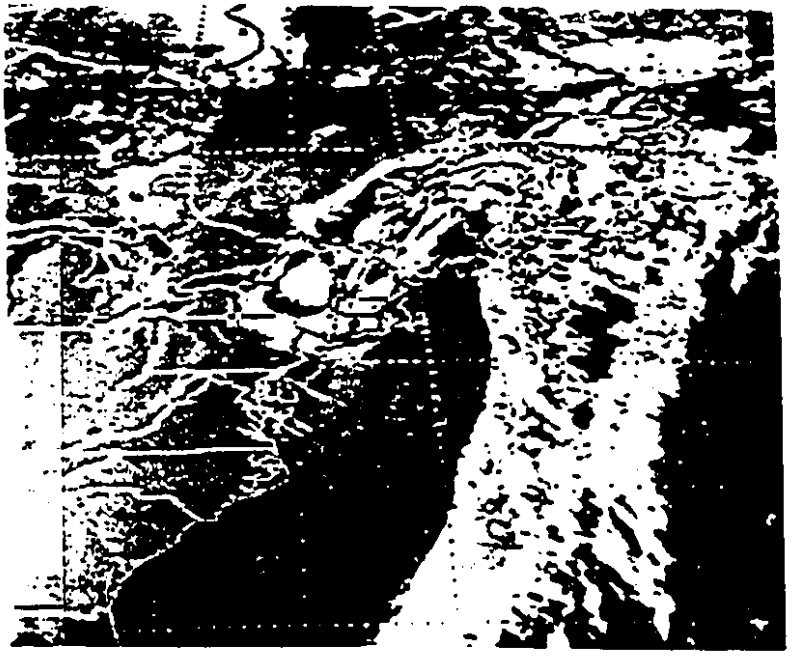

Fig. 3.3 (*Continued*)

a)

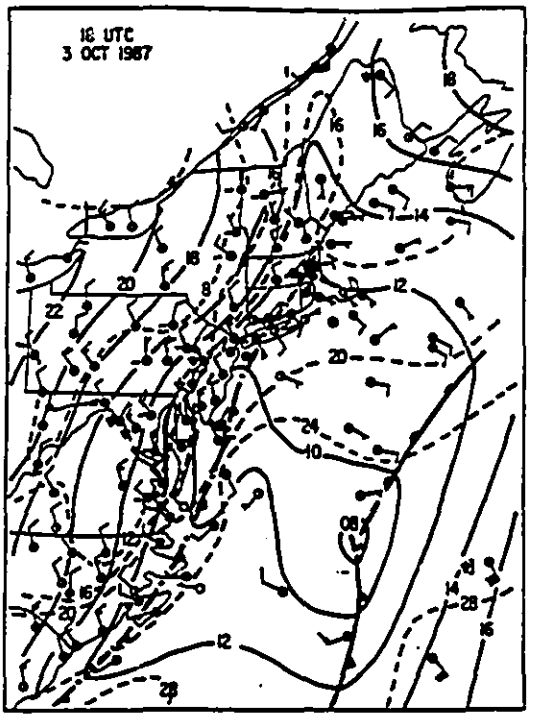

b)

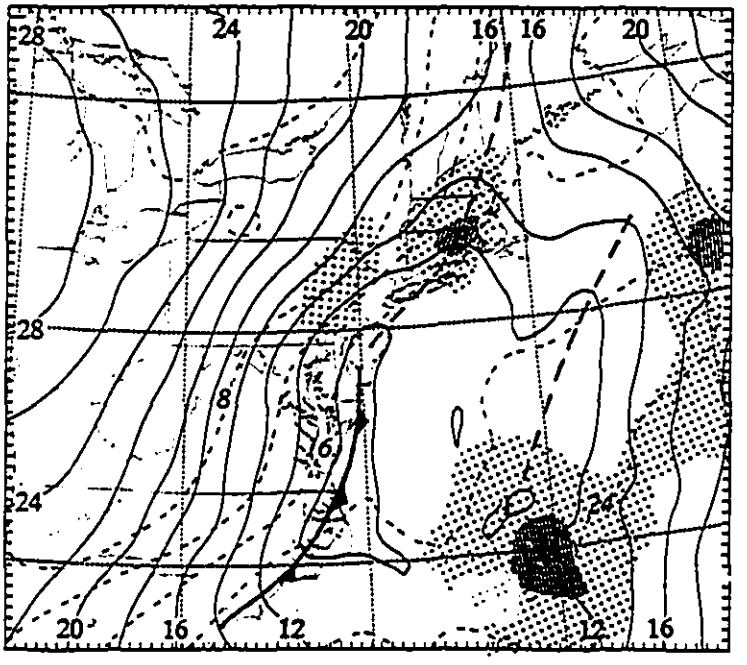

Fig. 3.4 Surface maps of mean-sea-level pressure (solid) at intervals of 2 hPa and temperature (dashed) at intervals of 4 °C for 1800 UTC 3 October 1987 from (a) the BS91 analysis; and (b) 6-h control simulation. Light and heavy shadings denote the past 3-h accumulated precipitation > 2 and > 8 mm, respectively; subjectively analyzed fronts and troughs are also shown .

the coastal front is also reasonably simulated (cf. Figs. 3.4a, b). However, the model is unable to simulate accurately the structure and intensity of the oceanic mesolow, although its movement is reasonably reproduced. This problem can be attributed to the lack of upper-air observations offshore in defining the system in the model initial conditions. Nevertheless, the model reproduces fairly well a widespread precipitation region associated with the oceanic system, as verified against the satellite imagery.

By 4/00-12 (Fig. 3.5a), the coastal cyclone deepened to 1004 hPa with closed isobars as it moved southeastward. This rapid genesis was accompanied by the intensifying cloud activity to the west of the cyclone, as shown by higher cloud tops in satellite imagery (cf. Figs. 3.3a, b). The northern tip of this cloud system, i.e., its "comma-shaped" head, had been rapidly advected off the coast of Newfoundland, and little further cloud development occurred in association with the parent cyclone to the north as it filled. On the other hand, the oceanic mesolow moved northeastward and it lost its identity gradually. However, its pertinent cloud activity was always much more extensive than that associated with the coastal cyclone.

The 12-h integration exhibits several features that are similar to the observed (cf. Figs. 3.5a, b). For example, the general area of cyclonic deepening, e.g., covered by the 1010-hPa isobar, resembles that in the BS91 analysis, including the orientation of the trough axis. The model also mimics well the increased area coverage and intensity of precipitation over the coastal region. Numerous three-hourly rainfall centers occur, e.g., off the North Carolina coast (8 mm), Long Island (12 mm) and southern New Hampshire (8 mm); over 65% are generated by the KF convective scheme. These rainfall centers correspond

a)

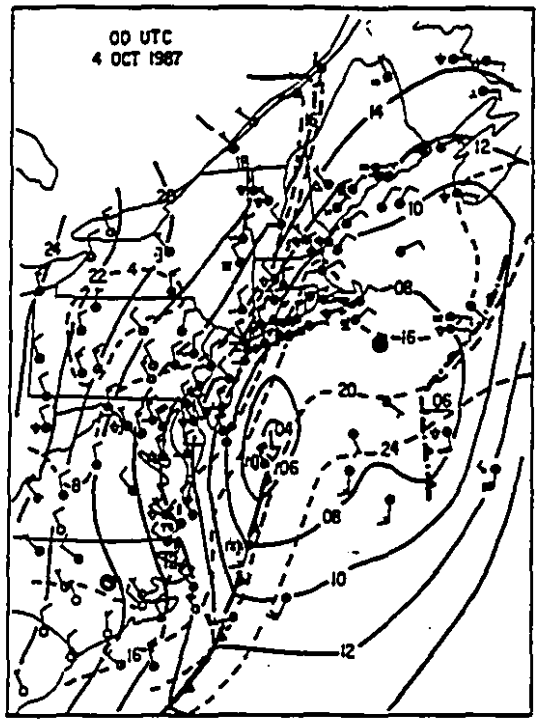

b)

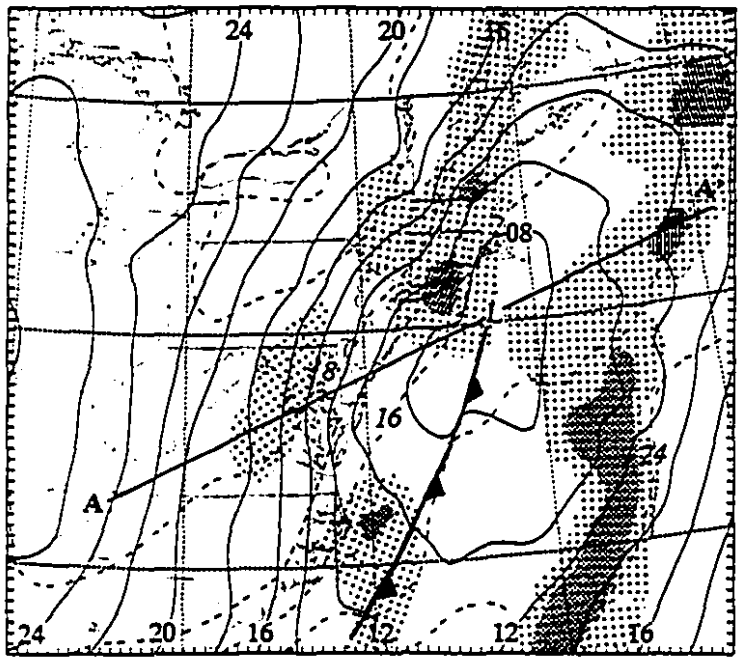

Fig. 3.5 As in Fig. 3.4 but for 4/00-12. Line AA' in (b) shows location of the cross section used in Fig. 3.10a.

reasonably well to the surface reports of thunderstorm activity over the regions (cf. Figs. 3.5a, b). The simulated extensive rainfall distribution associated with the oceanic system, mostly convective in nature, also compares favorably to that in the satellite imagery (cf. Fig. 3.3b).

While the large mesoscale circulation and precipitation structure are reasonably simulated, the model is unable to reproduce the right position and the right deepening of the coastal cyclone. A 5-hPa deepening was analyzed, as compared to the simulated 3-hPa deepening during the previous 6 hours (cf. Figs. 3.4 and 3.5). The difference in position can be attributed partly to the lack of high-resolution observations over the genesis region, particularly offshore, and partly to the fact that the genesis occurs in a weak-gradient and weak flow ambient ahead of the coastal front. We will show in section 4.2 how this difference in position could be responsible for the underprediction of the cyclone's intensity. Nevertheless, it is important that the MM4-simulated cyclone grows out of a frontal disturbance, rather than of the oceanic mesolow as in the NGM's forecast (Fig. 3.1).

In the following 12 hours, the coastal cyclone experienced a more rapid deepening (12 hPa in 12 h), after it changed its movement abruptly from southeast to north-northeast directions (Fig. 3.1). By 4/12-24, the cyclone reached its maximum intensity with a central pressure of 992 hPa after it just passed Boston (Fig. 3.6a). This resulted in a marked increase in the pressure gradient and wind speed in the cold sector, which in turn enhanced cold advection and eastward movement of the cold front. Associated with the rapid deepening was the intensified cloud activity (Fig. 3.3c) and increased precipitation in the cold sector (see Fig. 9 in BS91). Moreover, the precipitation type changed from rain to

a)

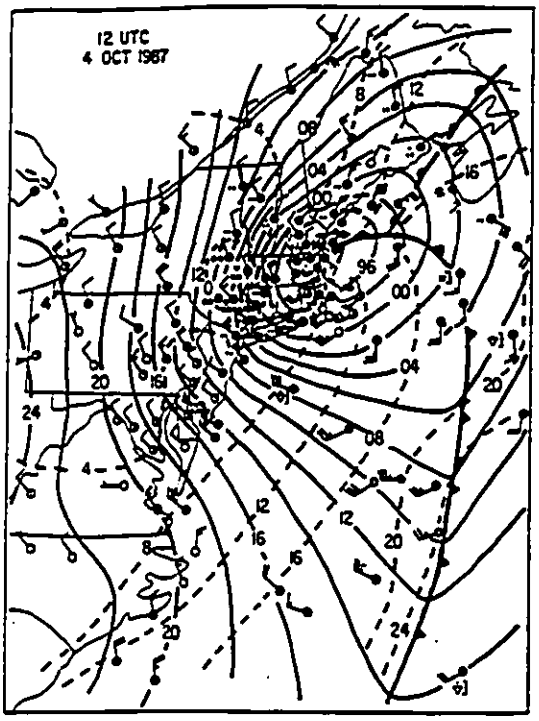

b)

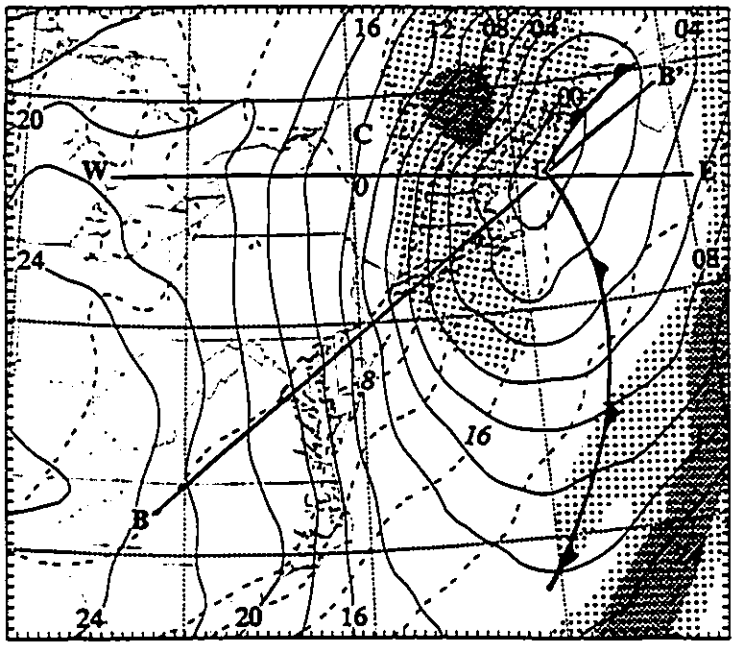

Fig. 3.6 As in Fig. 3.4 but for 4/12-24. Lines BB' and W-E in (b) show locations of the cross sections used in Figs. 3.10b and 3.11, respectively.

snow in eastern New York and western New England during this period. The corresponding satellite imagery (Fig. 3.3c) shows the merging of the two cloud systems into a "comma-shaped" system, which resembles in structure of the conveyor-belts cloud pattern as described by Carlson (1980). However, unlike the cold conveyor belt, the cloud system in the cold sector has very high cloud tops. The satellite imagery also shows a dry slot, nearly cloud-free, wrapping around into the cyclone center. As will be seen later from the MM4 simulation, this is caused by the descending motion associated with the tropopause depression that tends to advect the upper-level PV-rich air downward into the cyclone core.

The model captures reasonably well the more rapid genesis and the north-northeastward movement of the cyclone (Fig. 3.6b), although its deepening rate is underpredicted by 4 hPa during this 12-h period. As a result, pressure gradients in the cold sector intensifies and rainfall over the New England states increases, which are qualitatively in agreement with the BS91 analysis (cf. Figs. 3.6a, b). The simulated rainfall-free region near the cyclone center also conforms to the dry slot seen in the satellite imagery. It is of importance that the surface temperature, which was far above 0 ^{0}C 12-h earlier, now drops below 0 ^{0}C over northern New York due mainly to the cold advection behind the trough axis. Although the model produces little snow reaching the ground from stratiform clouds, melting and freezing are operative above 800 hPa. On the other hand, much of the observed snowfall might come from convective clouds, according to BS91 analysis, since only a few local stations reported surface temperatures below 0 ^{0}C (see Fig. 3.6a). This may explain, at least partly, why the model fails to reproduce the localized 0 ^{0}C isotherm over the heavy precipitation region. Nevertheless, a comparison of the simulation with a sensitivity run

withholding the ice microphysics reveals that the cooling by melting, as concerned by BS91, does not produce significant impacts on the evolution of the broad region of the 0 °C isotherm to the northwest and on the genesis and the final intensity of the coastal cyclone. Of course, the local cooling by melting must have played an important role in allowing snow to reach the surface (BS91).

Since the heavy snowfall (> 50 cm over eastern New York and western New England) made this storm an unusual early-season snow event according to BS91, it is particularly important to ascertain whether or not the MM4 model can reproduce reasonably the observed amount and distribution of the precipitation. In view of the lack of observations over the ocean, our verification is confined only to continental regions even though the oceanic rainfall is much more intense and extensive from the satellite imagery. Fig. 3.7 compares the MM4-simulated 24-h accumulated precipitation to the BS91 analyzed over the storm's whole life cycle between 0600 UTC 3 and 1800 UTC 4 October 1987. It is apparent that the model reproduces very well the basic distribution of precipitation, including the southwest to northeast orientation of heavy precipitation (cf. Figs. 3.7a, b). It is estimated from the BS91 analysis (i.e., their Fig. 9) that about 60% of the observed precipitation dropped during 0600 UTC 3 — 1200 UTC 4 period. With this in mind, one can see that the simulated area of precipitation amount > 20 mm, with its peak value > 60 mm, is close to the observed. Its pattern is, however, systematically shifted to the east of the observed owing to the error in the position of the simulated cyclone. About 30% of the precipitation over land is convective (see the dashed lines in Fig. 3.7b), which is more or less consistent with some surface reports of thunderstorms over the region. More

a)

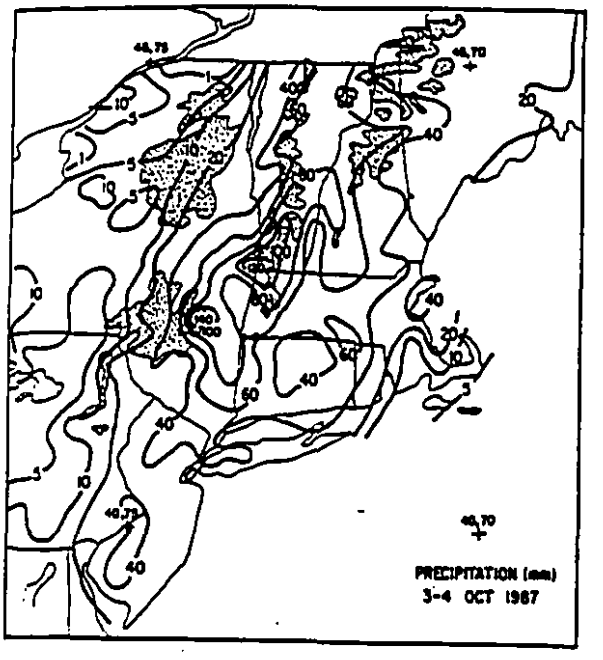

b)

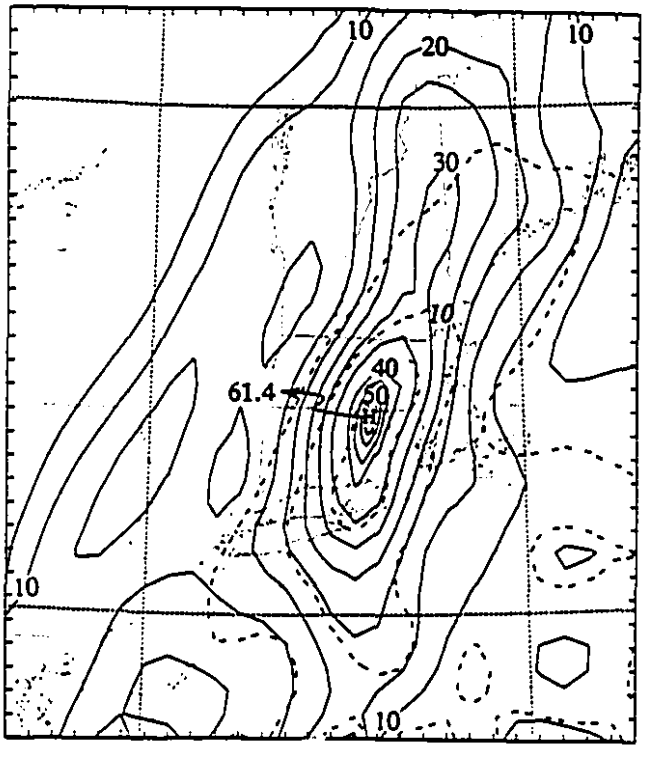

Fig. 3.7 Accumulated precipitation (mm) from (a) the BS91 analysis over the storm's whole life cycle between 0600 UTC 3 and 1800 UTC 4 October 1987; and (b) 24-h simulation (every 5 mm) of total precipitation (solid) and convective precipitation (dashed).

importantly, the simulated heavy rainfall event occurs entirely in the cold sector of the coastal cyclone, which differs from the classical warm- and cold-frontal type of precipitation as studied by previous researchers. This may help explain partly why the NGM failed to predict the heavy precipitation event over the coastal region, because i) the cyclone was predicted to grow out of a wrong perturbation, which tends to weaken the flow gradients in the cold sector; and ii) its subsequent propagation occurred too far offshore, which reduces the inshore transport of moisture, as will be shown in section 3.3.

3.2 Evolution of large-scale flow

As shown in Figs. 2.4a-c, the large-scale flow exhibits pronounced thermal advection in the lower troposphere with strong baroclinicity along the eastal coast and marked PV concentration at the base of the upper-level trough. Thus, it is desirable to examine how the large-scale flow responses to and guides the surface development.

It is found that a closed contour begins to form at the base of the 850-hPa trough after 6-h integration, in consistence with the surface development. By 4/00-12, the low has moved to the genesis region, with increased baroclinicity and thermal advection along the coast (Fig. 3.8c). The strong warm advection to the northeast of the cyclone can be seen from the rapid north-northwestward displacement of 8 — 16 ^{0}C isotherms in the warm sector during this 12-h period (cf. Figs. 2.4c and 3.8c). This advective process enhances the pre-existing frontal zone along the coastal region, with a warm front to the north and a cold front to the south of the cyclone. Associated with the strong thermal boundary is a high-PV zone extending from the primary cyclone over central Quebec southward into the north coast of

a)

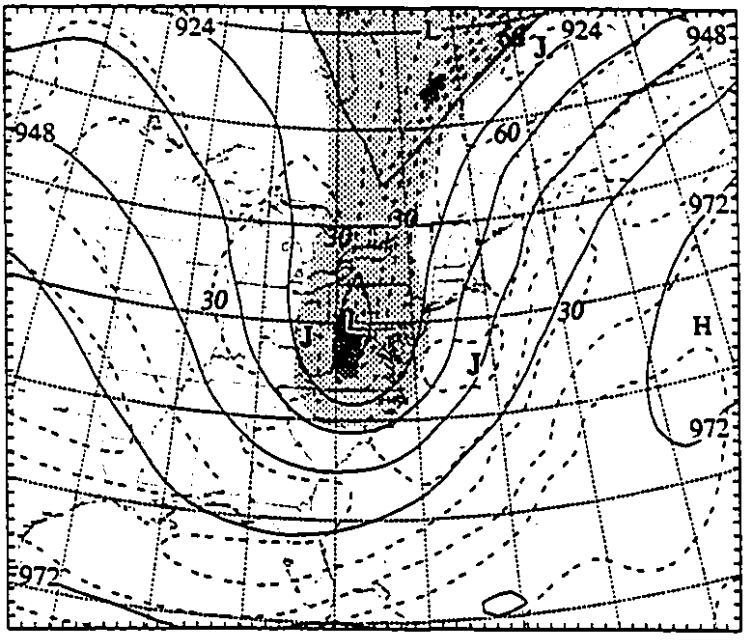

b)

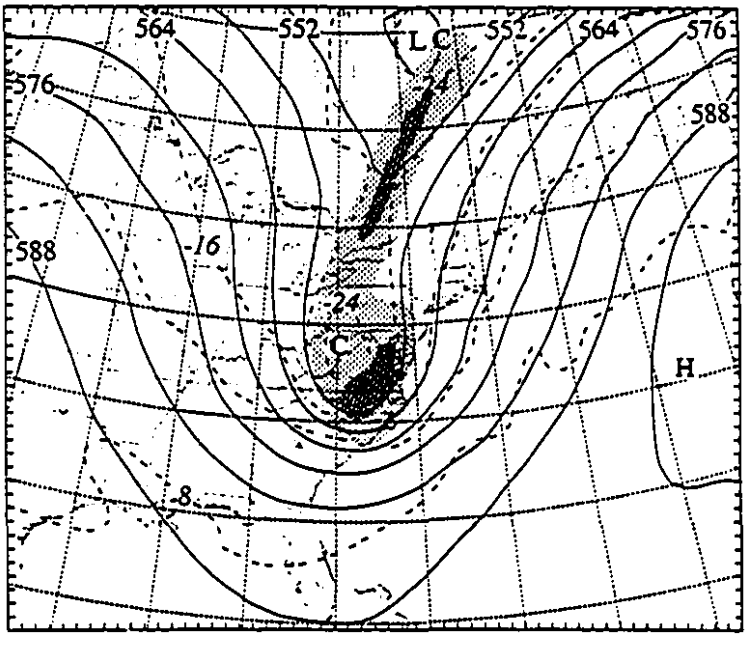

Fig. 3.8 As in Fig. 2.3 but from 12-h control simulation, valid at 0000 UTC 4 October 1987.

c)

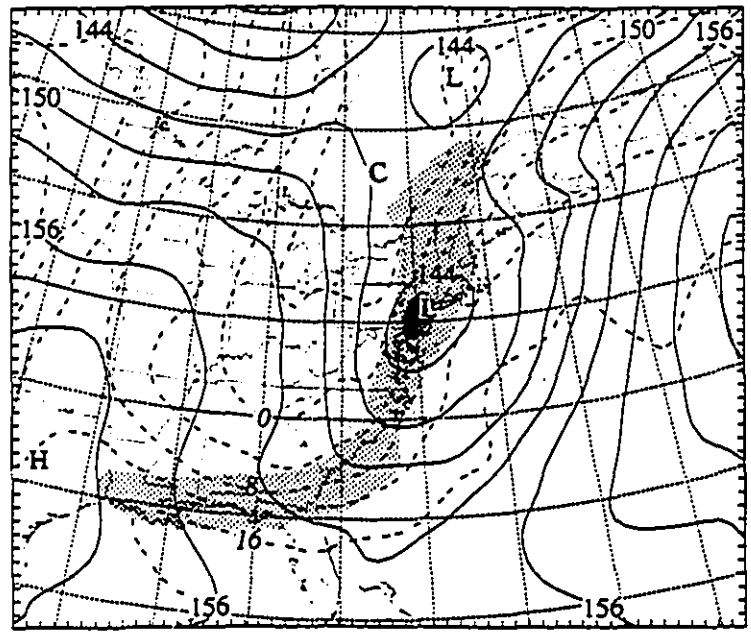

Fig. 3.8 (*Continued*)

the Gulf of Mexico, with a PV center, exceeding 2 PVUs, located in New Jersey.

In the middle to upper troposphere, the trough system moves rapidly eastward with little change in the pressure/thermal structures (cf. Figs. 2.4a,b and 3.8a, b). However, the PV concentration near the trough axis has intensified. An examination of Figs. 3.8a, b shows that this increase results from the descending of PV-rich air from the stratosphere in a vertically near-equivalent barotropic condition. This is evidenced by a 3 ^{o}C warming of the cold dome at 500 hPa in 12 hours, since little horizontal thermal advection occurs near the trough axis. On the other hand, the rapid eastward movement of the trough with respect to the surface cyclone reduces the vertical tilt of the baroclinic wave; the distance between the 500-hPa trough axis and the surface cyclone center has shortened from 750 to 500 km during the 12-h period (cf. Figs. 2.4 and 3.8). This implies that the upper-level PV or vorticity advection tends to play a more important role in the surface cyclogenesis as the trough approaches the coast.

At the end of the 24-h integration, i.e., at 4/12-24, the 850-hPa low intensifies considerably (Fig. 3.9c), as does the surface cyclone. A thermal ridge is built up near the low, which, from the PV-inversion viewpoint (Davis and Emanuel 1991), represents a positive thermal anomaly in the surface boundary condition that can be regarded as equivalent to a positive PV-anomaly contributing to the surface development. It is of interest to note that unlike typical cyclogenesis cases (e.g., Davis and Emanuel 1991; Reed et al. 1992), the low-level PV maximum does not coincide with the surface low. Rather, this high PV concentrates mainly in the cold sector where intense precipitation occurs. This appears to suggest that latent heat release in the present case may have less important contribution

a)

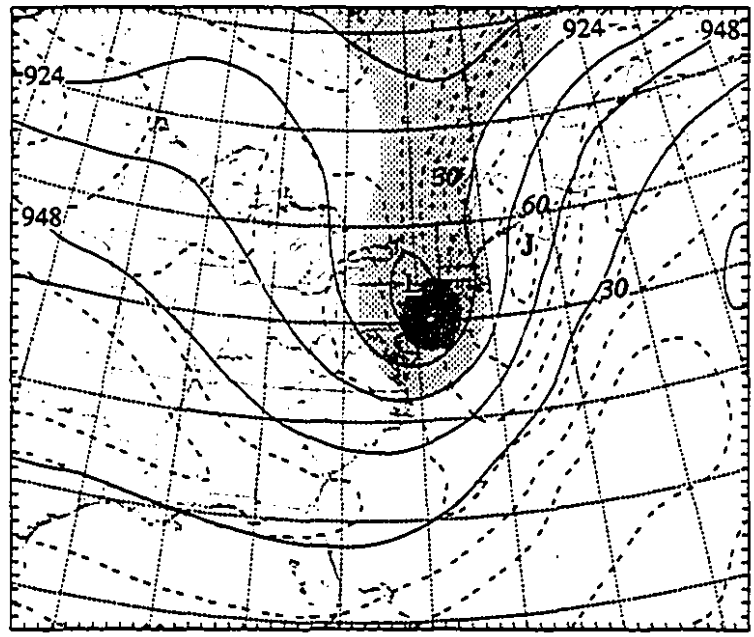

b)

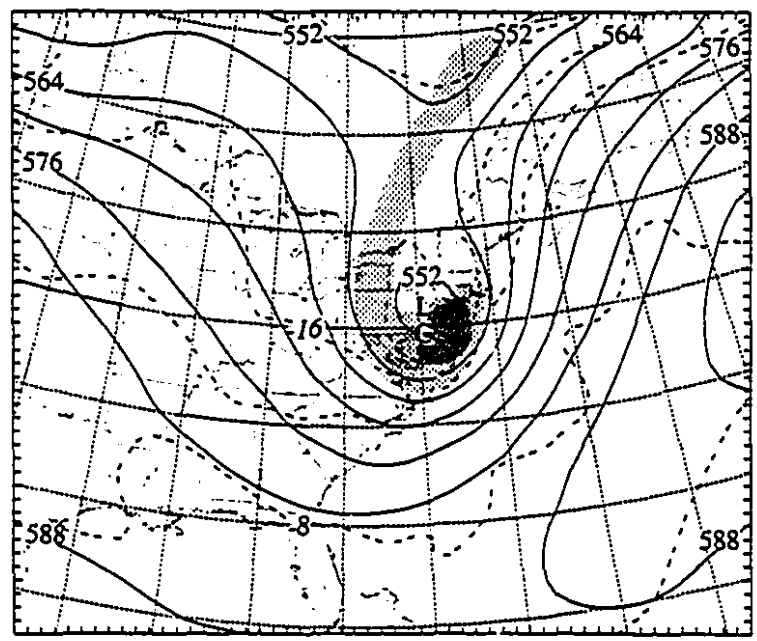

Fig. 3.9 As in Fig. 2.3 but from 24-h control simulation, valid at 1200 UTC 4 October 1987.

c)

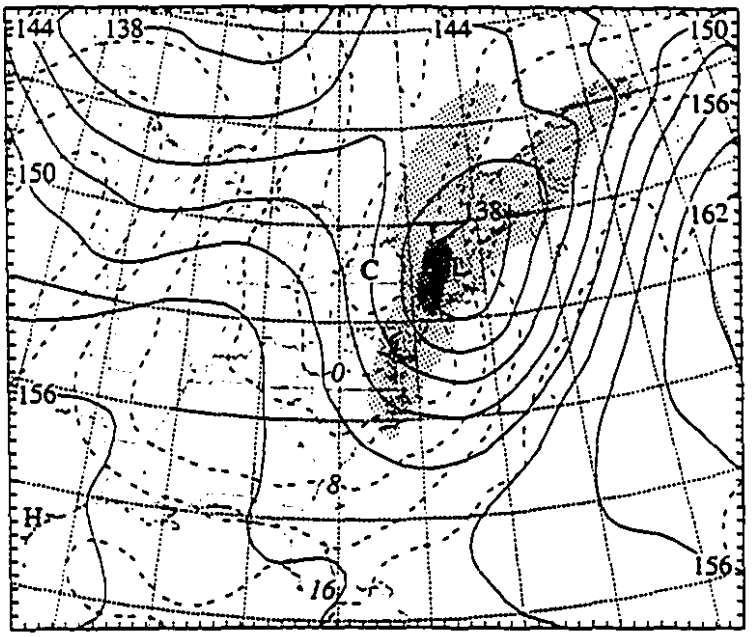

Fig. 3.9 (*Continued*)

to the cyclogenesis when the associated PV anomaly is inverted in accordance to Davis and Emanuel (1991).

Higher up, the PV anomaly at the base of the baroclinic trough continues to intensify as a result of advecting higher PV from the levels above, in agreement with the persistent warming of the cold dome (cf. Figs. 3.9a, b and 3.8a, b). Furthermore, the distance between the upper-level PV maximum and the surface cyclone has shortened considerably, leading to the further reduction of the vertical trough tilt. Meanwhile, the height gradients ahead of the trough axis increase, so does the associated southwest-to-southerly flow. Thus, the surface cyclone is now in a more favorable position for being influenced by the upper-level PV anomaly, corresponding to the most intense stage of the coastal cyclone. On the other hand, the surface cyclone has entered into the left entrance region of the upper-level jet streak (cf. Figs. 3.8a and 3.9a), implying the presence of an unfavorable environment for the surface development. Moreover, the cyclone moves more rapidly north-northeastward, under the steering of the upper-level intensified flow, into the colder continental region having stronger frictional damping and less moisture supply. All these factors suggest that the cyclone tends to decay hereafter.

3.3 Vertical structure of the cyclone

Tc gain insight into the vertical coupling of the upper- and low-level disturbances, Figs. 3.10a, b show the vertical structure of PV and potential temperature, superposed with along-plane flow vectors, at two different stages of the cyclone development. They were taken through the upper-level PV core and the surface cyclone center roughly along the 300-

hPa southwesterly flow. Hoskins et al. (1985) have provided a review of the usefulness of PV analysis in understanding the nature of extratropical cyclogenesis. Davis and Emanuel (1991) have discussed the relative importance of upper-level PV anomalies associated with the tropopause depression, cloud-induced low-level PV anomalies and surface warmth in the cyclogenesis.

There are clearly two distinct PV concentrations in the vertical: one centered at 300 hPa in the dry air (RH < 30%) and the other in the 950-800 hPa layer within the cloudy air (RH > 90%). The low-level PV, exceeding 3 PVUs, is mainly confined in the frontal zone in association with the stratiform precipitation. Much weaker and shallower PV is, however, located above the surface low owing to the development of little precipitation over the region, as also indicated by lower relative humidity and weaker ascending motion (Fig. 3.10b). In the upper troposphere, the downward penetration of stratospheric high-PV air, or the tropopause depression, in conjunction with the subsidence of the cold dome is evident. By 4/12-24, a deep layer of the stratospheric air has been descended into the trough region, with the lowest tropopause reaching 500 hPa and below (see the 2-PVU contour). Like the upper-level trough structure, the upper-level PV anomaly is being advected toward the surface cyclone, shortening the distance between the two from about 550 km at 4/00-12 to less than 150 km at 4/12-24 (cf. Figs. 3.10a, b). This indicates again the growing importance of the upper-level PV anomaly (or troughs) in the surface cyclogenesis toward the later stages of the cyclone development. Of course, the quantitative effect of the upper-level PV anomaly can only be evaluated through a piecewise PV inversion as proposed by Davis and Emanuel (1991).

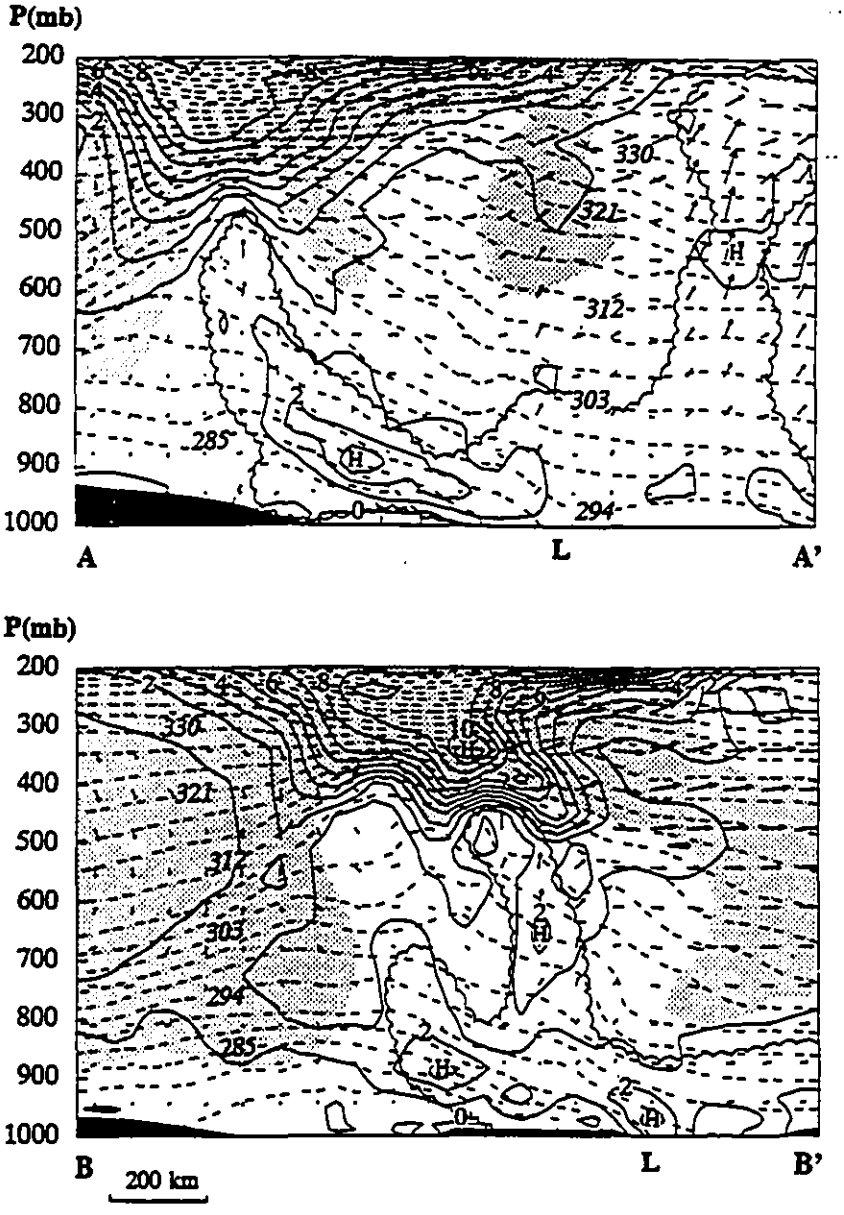

Fig. 3.10 Vertical cross sections of potential vorticity (solid) at intervals of 1 PVU and potential temperature (dashed) at intervals of 3 K, superposed with along-plane flow vectors from (a) 12-h; and (b) 24-h control simulations. They are taken along lines AA' and BB' given in Figs. 3.5b and 3.6b, respectively. Shading denotes relative humidity < 30% whereas scalloped lines show relative humidity > 90%. The position of the cyclone center is indicated by "L" on the abscissa.

Fig. 3.11 shows the vertical baroclinic structures of the coastal cyclone at the end of the 24-h integration, using a west-east cross section of height and temperature deviations. All deviations are obtained by subtracting their pressure-level averages in the cross section. It is seen that the height trough tilts westward up to 600 hPa, and then a changeover to near-equivalent barotropics occurs aloft. Likewise, the westward tilt of the thermal perturbation is only confined to the lower troposphere, but with a baroclinically favorable phase lag with the height trough. These vertical structural relationships are more pronounced at the early stages of the cyclogenesis. Although a deep layer of strong thermal gradients appears in the vicinity of the coastal cyclone, the system-relative wind vectors suggest that more pronounced warm advection contributing to the cyclone's deepening only occurs in the lowest 300-hPa layer.

To examine how so much precipitation could be generated in the cold sector, Fig. 3.12 displays the vertical structure of equivalent potential temperature, θ_e, superposed with in-plane flow vectors along a west-east cross section about 150 km to the north of the cyclone center. This cross section shows the source of latent energy feeding the cyclone. There are a narrow region of strong ascent at the leading frontal boundary and a wide region of slantwise ascent up to 400 hPa at the back edge of the stratiform region (also see Figs. 3.10b and 3.11). However, little or very weak ascent occurs in the potentially unstable region in the warm sector. The flow vectors suggest that the potentially unstable air is being transported into the frontal zone, where both the upright and slantwise liftings to saturation occur and the instability is released. Of significance is that the slantwise transport of the high-θ_e air from the maritime boundary layer has generated a mid-level potentially unstable

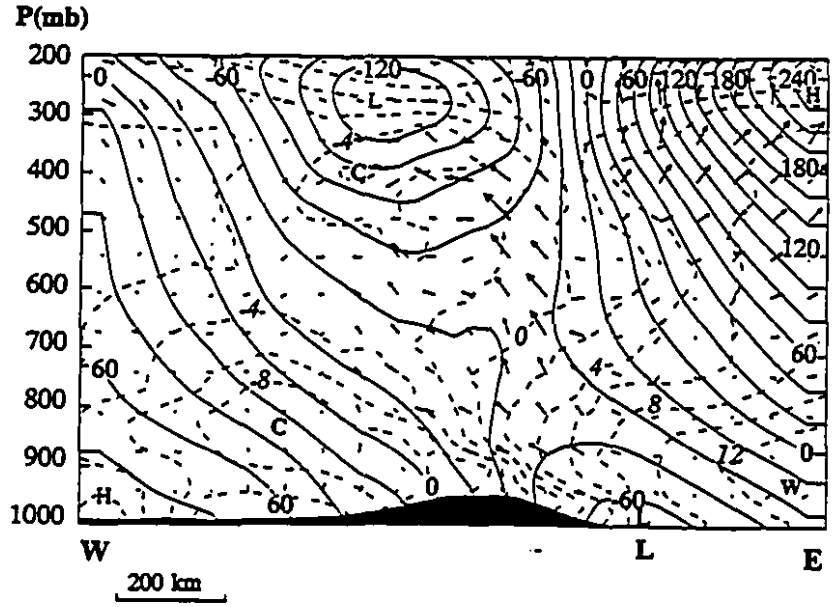

Fig. 3.11 West-east vertical cross section of height deviations (solid) at intervals of 20 m and temperature deviations (dashed) at intervals of 2 °C, superposed with along-plane system-relative flow vectors, from 24-h control simulation. It is taken along line W-E given in Fig. 3.6b. The position of the cyclone center is indicated by "L" on the abscissa.

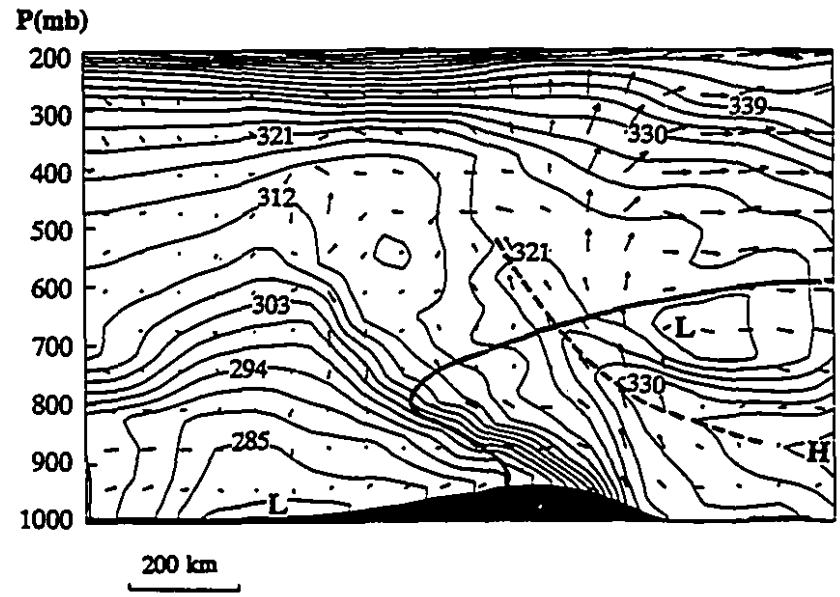

Fig. 3.12 Vertical cross section of equivalent potential temperature, θ_e, at intervals of 3 K, superposed with along-plane flow vectors from 24-h control simulation, which is taken along a line 150 km north of the line W-E in Fig. 3.6b. Thick solid line denotes 0 °C isotherm in the plane.

layer above the frontal zone. Similar features also appear in the northerly return flow slightly to the southwest of the cyclone center, as the high-θ_e air is advected cyclonically in the cold sector. The results reveal that the warm and humid maritime boundary layer is the energy (moisture) source to the precipitating system, and the upright and slantwise liftings of the associated high-θ_e air over the frontal zone are responsible for a variety of the reported weather phenomena, such as thunderstorms, freezing rain and snowfalls.

In summary, the coastal cyclone is initiated in a polar frontal zone and then it intensifies in a favorable large-scale environment with pronounced warm advection in the lower troposphere and significant PV concentration in the upper troposphere. The transport of warm and moist air from the maritime boundary layer into the frontal zone accounts for the observed heavy precipitation in the cold sector. In the next chapter, we will examine the relative importance of latent heat release, low-level thermal advection and upper-level PV advection during the different stages of the cyclone development.

Chapter 4

Genesis Mechanisms and Numerical Predictability

As discussed in the preceding chapter, the low- to mid-level thermal advection, the upper-level PV forcing associated with the tropopause depression and latent heat release all appear to have played important roles in the present cyclogenesis event. In this chapter, we examine to what extent these different processes contribute to the cyclogenesis during different stages of the cyclone's life cycle, in order to gain some insight into the numerical predictability of the storm. All this will be done through analyses of the high-resolution simulations. Section 4.1 shows the different effects of the upper- and lower-level adiabatic processes versus diabatic heating on the cyclogenesis. Results are then used in section 4.2 in conjunction with some sensitivity simulations to investigate the impacts of different initial conditions and other factors on the predictability of the coastal cyclone.

4.1 Effects of diabatic versus adiabatic processes

To isolate the effects of large-scale baroclinic forcings versus diabatic heating on the coastal cyclogenesis, a sensitivity simulation was performed, in which both convective and grid-scale condensation were excluded (Exp. DRY) while keeping all the other model physical parameters identical to the control simulation (Exp. CTL, or moist). Without the forcing from the diabatic heating, the model atmospheric circulations are only dominated by

advective processes. Thus, any difference between the dry and moist runs can be attributed to the release of latent heat.

a. Effect of diabatic heating

It is apparent from Fig. 3.1 that without the diabatic heating, the track of the dry cyclone follows closely that of the moist one, except for its relatively slower movement. This implies that dry dynamics determines the track of the coastal cyclone whereas moist processes influence the speed of movement. It is also apparent from Fig. 3.2 that the dry cyclone is generally weaker than the moist one, except for the first 6-h period in which little difference occurs owing to the development of weak and scattered precipitation in the cold sector (see Fig. 3.4b). The dry cyclone is about 4 hPa weaker than the moist one at the end of the 24-h integration, indicating that diabatic heating only accounts for 28% of the total deepening. The slower movement and weaker intensity of the dry cyclone have been found to be common features by previous studies of oceanic cyclogenesis (e.g., Aubert 1957; Anthes and Keyser 1979; Chang et al. 1982; Kuo and Reed 1988). However, the results are in significant contrast with the coastal cyclogenesis studies by Lapenta and Seaman (1992) and Doyle and Warner (1992), who showed that the coastal cyclone fails to develop when latent heating was withheld. Moreover, the life cycle of the dry cyclone in the present case is nearly the same as the moist one, i.e., a slow deepening in the first 12-h followed by a more rapid deepening period. It follows that the large-scale dry dynamics dictates the genesis and its subsequent rapid deepening of the present coastal storm, whereas the diabatic heating only plays a role in modulating the cyclogenesis processes (Davis et al. 1993).

The above conclusion can be further seen from the simulated 24-h surface maps

between the dry and moist cyclones (cf. Figs. 4.1a and 3.6b). The basic circulation characteristics of the two are very similar to each other, except for a greater horizontal extent, as indicated by the 1012-hPa isobar, and a slightly stronger pressure gradient in the vicinity of the moist cyclone. Of importance to note is that the dry simulation also reproduces the 0 ^{0}C isotherm in northern New York as observed. This reveals further that the broad area of the 0 ^{0}C isotherm results mainly from the cold advection in the north-to-northeasterly return flow. To test further the significance of diabatic heating, we have conducted a sensitivity simulation, in which a deep layer in the cold sector was substantially moistened in accordance to the cloud distribution visible from the satellite imagery. It is found that the model only produces a slight deepening of the cyclone at the end of the 24-h integration (not shown).

The much less significant impact of diabatic heating in the present case may be partly attributed to the fact that the majority of precipitation falls in the cold sector in the cyclonic return flow, unlike those classical cases in which a large quantity of rainfall occurs along a warm front to the left or ahead of the cyclone track (e.g., Anthes and Keyser 1979; Kuo et al. 1991; Lapenta and Seaman 1992). Specifically, from a PV perspective, latent heat release will produce a positive PV anomaly below the heating maximum and its efficiency of influence on cyclogenesis depends on the radial and vertical distribution of the heating or PV anomaly (see Hack and Schubert 1986). Since in the present case such a PV anomaly occurs in the cyclonic return flow (see Figs. 3.8c and 3.9c), it tends to be advected southward away from the cyclone center. On the other hand, the precipitation associated with the oceanic system, mostly convective, produces a PV anomaly above 600 hPa (see Fig.

a)

b)

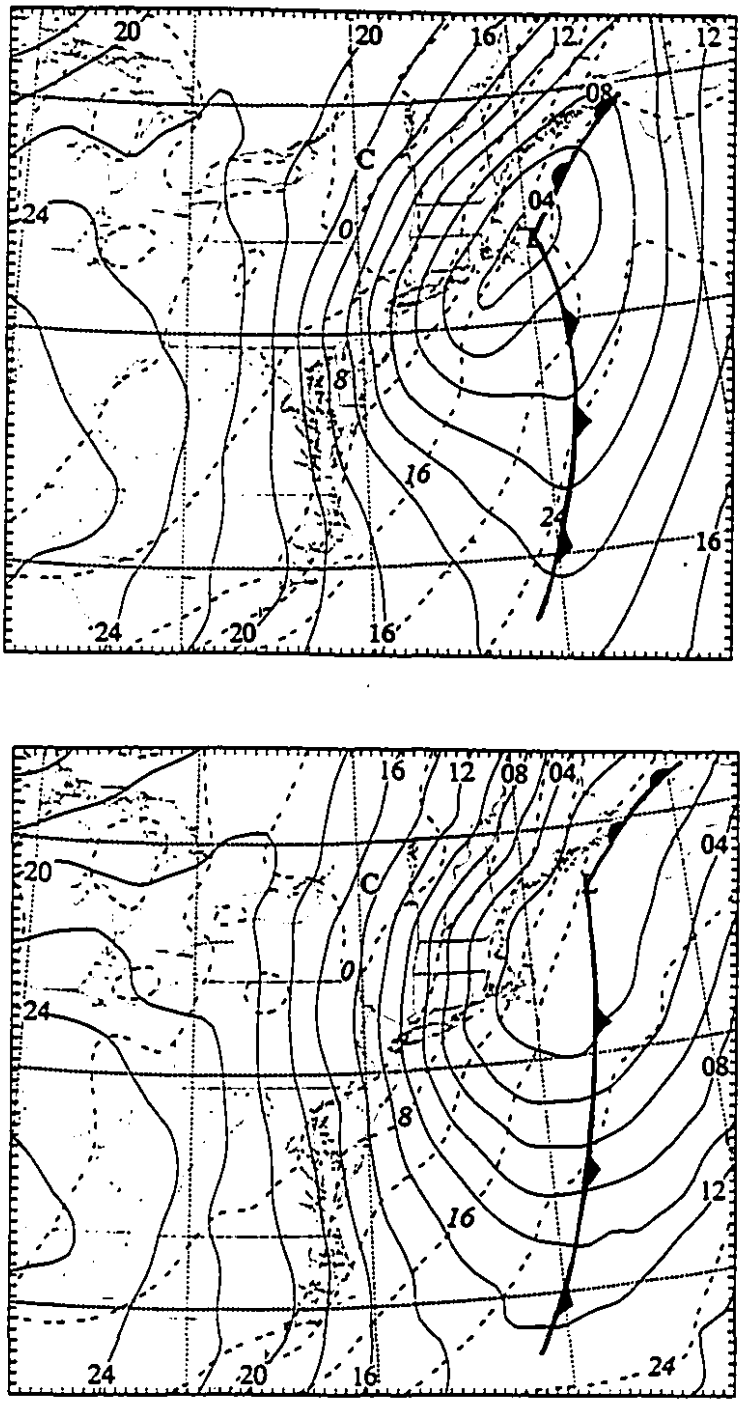

Fig. 4.1 Surface maps of mean-sea-level pressure (solid) at intervals of 2 hPa and temperature (dashed) at intervals of 4 °C from 24-h integrations of (a) Exps. DRY and (b) NBG; (c) 12-h integration of Exp. I12; and (d) 24-h integration of Exp. NUG, all ending at 1200 UTC 4 October 1987. Line CC' in (d) shows location of cross section used in Fig. 4.5; subjectively analyzed fronts are also given.

c)

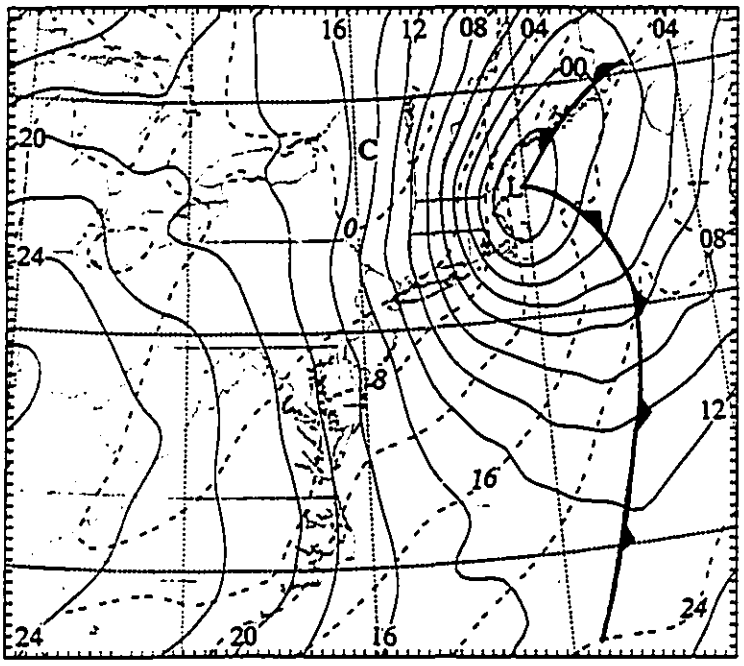

d)

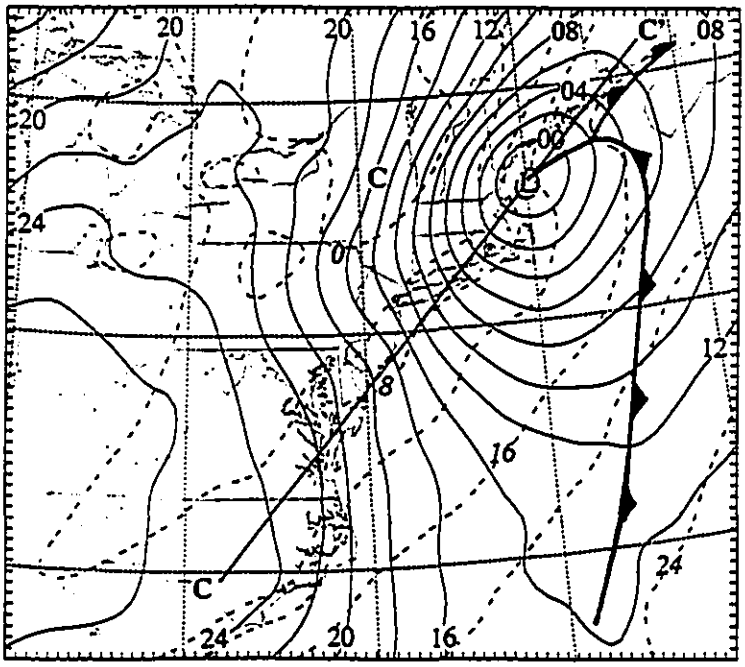

Fig. 4.1 (*Continued*)

3.10a), which tends to be advected northeastward away from the cyclone center. Thus, the heating-induced PV anomalies have less chance to contribute persistently to the cyclogenesis from a PV-inversion viewpoint.

b. Relative importance of the upper- and low-level adiabatic processes

After seeing that the dry dynamics accounts for the genesis and a large portion of the final depth of the cyclone, it is desirable to examine the individual contributions of upper- and low-level adiabatic processes to the cyclogenesis. This can be done through diagnostic analyses of the dry simulation using the simplified Zwack-Okossi development equation (Lupo et al. 1992; henceforth Z-O). The Z-O equation provides a complete description of all the forcing contributions at any level to the geostrophic vorticity changes at the surface or any pressure level close to the surface. The modified Z-O equation is given by Lupo et al. (1992) as follows

$$\frac{\partial \zeta_{gl}}{\partial t} = Pd\int_{P_t}^{P_l} (-\boldsymbol{V}\cdot\nabla\zeta_a)\, dp - Pd\int_{P_t}^{P_l} [\frac{R}{f}\int_{p}^{P_l}\nabla^2 (-\boldsymbol{V}\cdot\nabla T + \frac{Q}{c_p} + S\omega)\, \frac{dp}{p}]\, dp$$
$$+ Pd\int_{P_t}^{P_l} \boldsymbol{k}\cdot\nabla\times\boldsymbol{F}dp - Pd\int_{P_t}^{P_l} \frac{\partial \zeta_{ag}}{\partial t}\, dp\ , \qquad (4.1)$$

where ς_{gl} is the geostrophic vorticity at level l; p_l and p_t are pressure at the bottom and top levels of a column, respectively; $Pd = (p_l - p_t)^{-1}$; ς_a (= ς + f) denotes the absolute vorticity; Q represents the diabatic heating rate; S is the static stability parameter, defined as $S = -(T/\theta)(\partial\theta/\partial p)$; F denotes the friction force; and other variables have their conventional meaning. The vertical motion in p-coordinates, ω, is calculated using the omega equation

derived by Tsou and Smith (1990),

$$[\nabla^2\sigma + f(\zeta + f)\frac{\partial^2}{\partial p^2}]\omega = f\frac{\partial}{\partial p}(\boldsymbol{V}\cdot\nabla\zeta_a) + \frac{R}{p}\nabla^2(\boldsymbol{V}\cdot\nabla T) - \frac{R}{p}\nabla^2(\frac{Q}{c_p}) + f\frac{\partial}{\partial p}(\boldsymbol{k}\cdot\nabla\times\boldsymbol{F}) \quad . \tag{4.2}$$

It is evident from Eq. (4.2) that the development of vertical motion consists of the contributions from four elements, namely, due to vertical differential vorticity advection (ω_v), the Laplacian of thermal advection (ω_T) and diabatic heating (ω_Q), and the vertical friction-induced vorticity flux divergence (ω_F).

In the dry case, the diabatic heating terms in Eqs. (4.1) and (4.2) vanish. If the vorticity tendency is calculated at p_1 = 950 hPa, the frictional effects over the ocean are small and so they can be neglected. Thus, with the relation of $\varsigma = \varsigma_g + \varsigma_{ag}$, Eqs. (4.1) and (4.2) can be rewritten as

$$\frac{\partial\zeta_1}{\partial t} = Pd\int_{P_t}^{P_1} -\boldsymbol{V}\cdot\nabla\zeta_a\,dp - Pd\int_{P_t}^{P_1}[\frac{R}{f}\int_{p}^{P_1}\nabla^2(-\boldsymbol{V}\cdot\nabla T + S\omega)\frac{dp}{p}]\,dp - Pd\int_{P_t}^{P_1}\frac{\partial\zeta_{ag}}{\partial t}\,dp + \frac{\partial\zeta_{ag1}}{\partial t} \quad , \tag{4.3}$$

$$[\nabla^2\sigma + f(\zeta + f)\frac{\partial^2}{\partial p^2}]\omega = f\frac{\partial}{\partial p}(\boldsymbol{V}\cdot\nabla\zeta_a) + \frac{R}{p}\nabla^2(\boldsymbol{V}\cdot\nabla T) \quad . \tag{4.4}$$

Tsou et al. (1987) found that the third term on the right hand side (RHS) of Eq. (4.3), i.e., the ageostrophic vorticity tendency, is small on the synoptic scale. Since the last two terms on the RHS of Eq. (4.3) are on the same order of magnitude but opposite in sign, they can

be neglected for the present dry run. Therefore, the Z-O vorticity budget equation can be further simplified as

$$\frac{\partial \zeta_1}{\partial t} = Pd\int_{P_t}^{P_1}[-V\cdot\nabla\zeta_a - \frac{R}{f}\int_{P}^{P_1}\nabla^2 S\omega_\zeta \frac{dp}{p}]\,dp \qquad (A)$$
$$- Pd\int_{P_t}^{P_1}[\frac{R}{f}\int_{P}^{P_1}\nabla^2(-V\cdot\nabla T + S\omega_T)\frac{dp}{p}]\,dp, \qquad (B) \qquad (4.5)$$

where p_t = 100 hPa is used to include some potential effects of the lower stratosphere. Term A represents the column-integrated contribution of horizontal vorticity advection to the vorticity tendency at the bottom of the column, whereas term B is the column-integrated contribution from the Laplacian of horizontal temperature advection. Note that the individual adiabatic effects induced by pure vorticity and thermal advections have been included into terms A and B, respectively. It is found that the induced adiabatic cooling or warming effects on the vorticity tendency are negatively correlated with the advective vorticity and thermal contributions (not shown).

The vorticity budget calculations begin by solving the ω-equation with the two separate forcings in Eq. (4.4) using successive over-relaxation, assuming zero vertical and lateral boundary conditions. The two different contributions are then added to the corresponding terms in Eq. (4.5) to produce the total vorticity tendency at 950 hPa.

Figs. 4.2 and 4.3 show the column-integrated vorticity budgets at 4/00-12 and 4/12-24, respectively, representing the two different stages of the cyclone development. A well-organized couplet of positive/negative tendencies is seen ahead of and behind the cyclone,

a)

b)

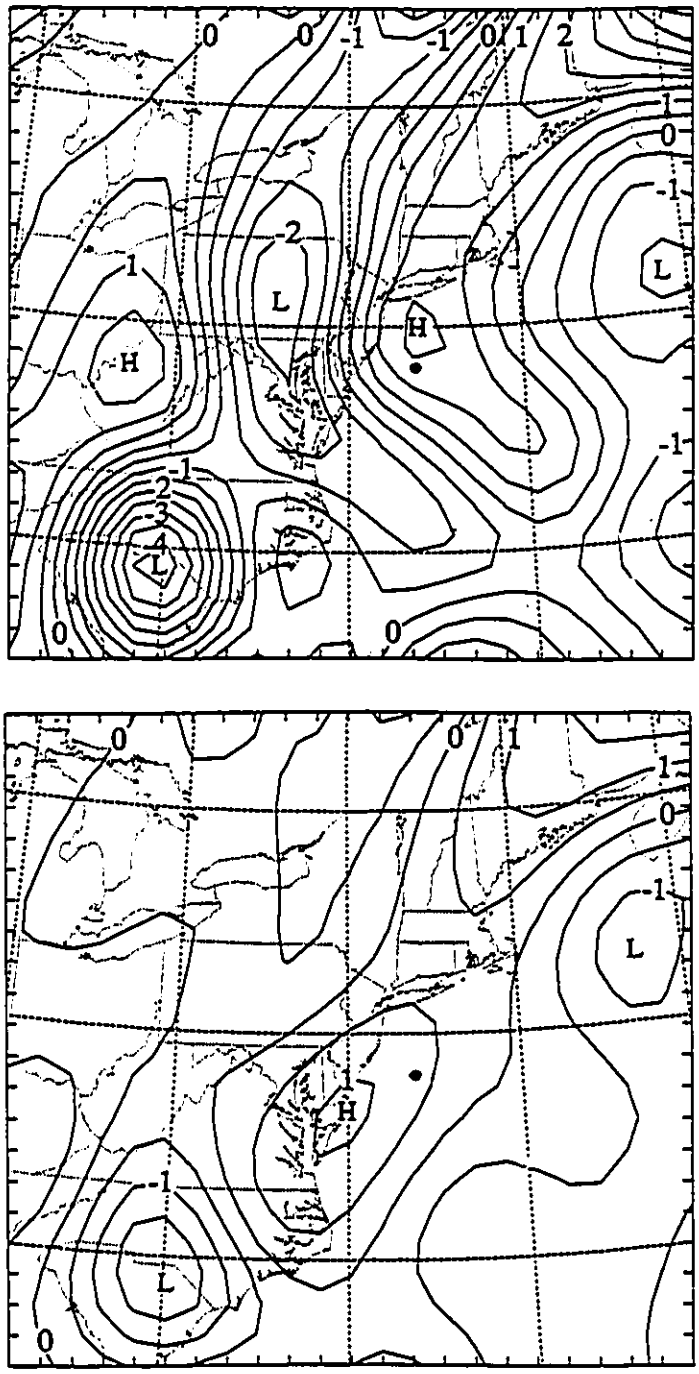

Fig. 4.2 Horizontal maps of the column-integrated budget at 950 hPa: (a) net vorticity tendency; (b) contribution of horizontal vorticity advection; and (c) contribution of Laplancian of horizontal temperature advection, at intervals of 0.5 × 10^{-9} s^{-2} from 12-h integration of Exp. DRY, valid at 0000 UTC 4 October 1987. The solid circle, "•", denotes the grid point with the minimum sea-level pressure in Exp. DRY.

c)

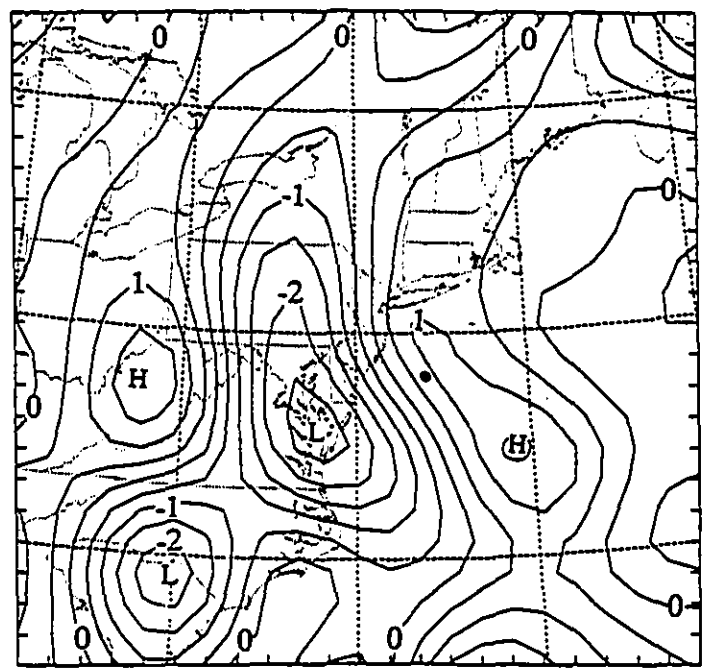

Fig. 4.2 (*Continued*)

a)

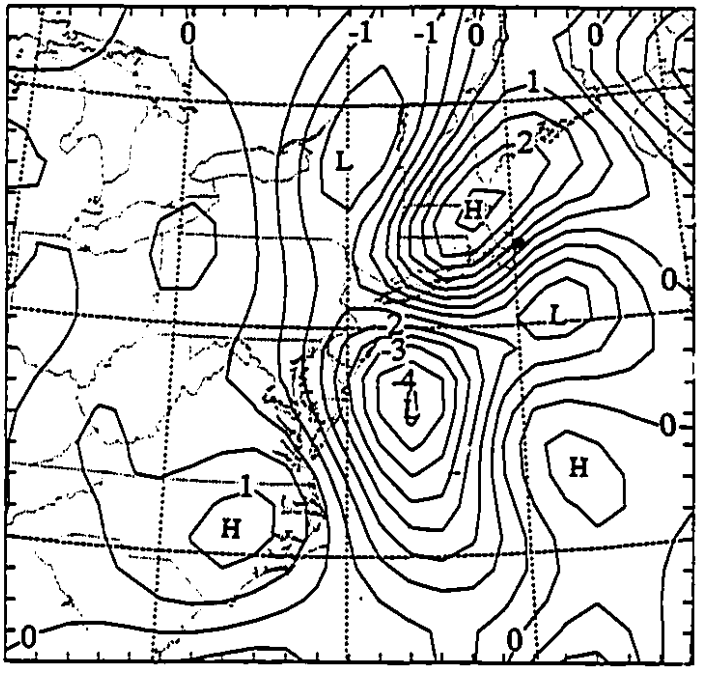

b)

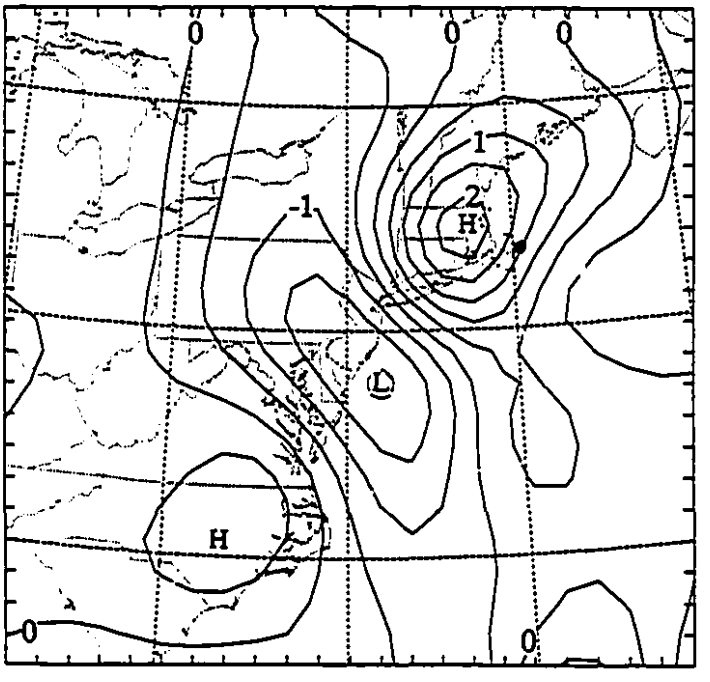

Fig. 4.3 As in Fig. 4.2 but for 24-h integration, valid at 1200 UTC 4 October 1987.

c)

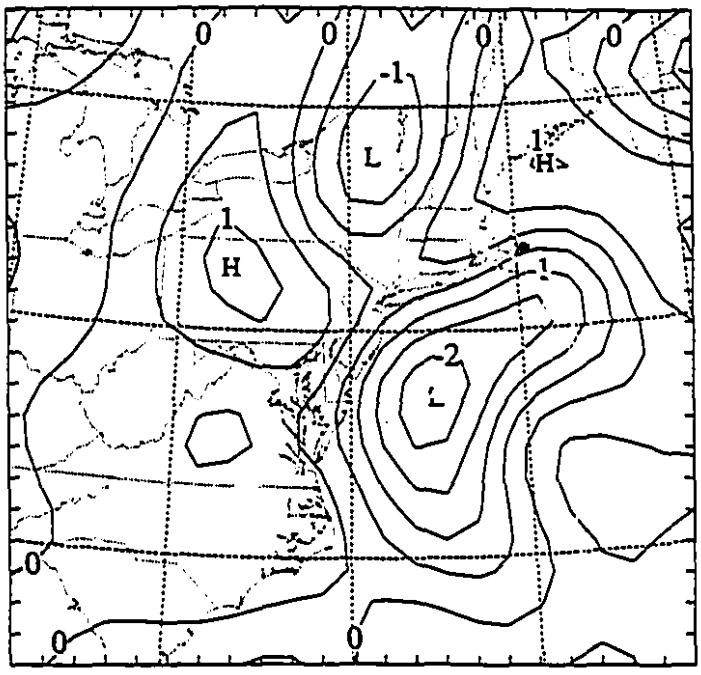

Fig. 4.3 (*Continued*)

which is typically the propagating characteristics of a vorticity center. The positive tendency center gives roughly the location to which the cyclone's vorticity center at 950 hPa is about to propagate. Note that the vorticity tendency peak increases from 1.6×10^{-9} s^{-2} at 4/00-12 to 2.7×10^{-9} s^{-2} at 4/12-24, which is consistent with the more rapid deepening rate of the system as it enters into the mature stage (cf. Figs. 3.2, 4.2a and 4.3a).

It is evident that the column-integrated vorticity advection always produces positive contributions to the cyclogenesis as long as the genesis takes place in the downstream of the upper-level trough (see Figs. 4.2b and 4.3b). Its along-coastal distribution appears to determine the general SW-NE oriented track of the cyclone given in Fig. 3.1. Its magnitude depends on the vertical slope of the trough tilt, and it is maximized when the low- and upper-level vorticity centers are vertically coherent. This explains why the contribution of the vorticity advection *doubles* at the end of the second 12-h integration. Likewise, the column-integrated contributions due to the Laplacian of thermal advection are positive (i.e., warm advection) in the southerly flow, mostly over the ocean (see Figs. 4.2c and 4.3c). As compared to the vorticity advection, however, both the extent and the change in the magnitude of the thermal contribution are relatively small during the storm's life cycle, and its contribution *decreases* as the system enters the mature stage. More significant changes take place in the structure of the thermal contribution. Specifically, at the cyclone's early stages, an extensive area of positive thermal contribution occurs in the warm sector, more pronounced to the southeast of the cyclone center. This is more associated with the warm advection of oceanic air mass by the low-level inshore cyclonic circulation over the broad low-pressure region (cf. Figs. 3.5, 3.8c and 4.2c). After entering the mature stage, the

positive thermal contribution, although still remaining inshore, shrinks in size and appears only to the north of the cyclone center.

Table 4.1 Relative contribution (%) of the column - integrated contribution due to the vorticity advection (Term A) and temperature advection (Term B) to the net vorticity tendency at 950 hPa that are averaged over an area of 75 km x 75 km over the cyclone center

	3/18-06	4/00-12	4/06-18	4/12-24
Term A	41	42	76	85
Term B	59	58	24	15

Of our major concern here is the relative contributions of the vorticity and thermal advection to the cyclogenesis. For this purpose, Table 4.1 lists the 6 hourly relative contributions of the (upper-level) vorticity advection and the Laplacian of the (low-level) thermal advection to the net vorticity tendency that are averaged over an area of 75 km × 75 km near the cyclone center. It is apparent that the lower-level thermal advection accounts for 59% of the total deepening in the first 12 hours and it decreases rapidly afterward. By comparison, the relative importance of the vorticity advection is relatively small during the incipient stage but it becomes more and more dominant as the storm enters the mature stage. Thus, the quasi-geostrophic development principle hypothesized by BS91 appears to operate more efficiently during the mature stages of the coastal cyclogenesis, since the upper-level

vorticity advection determines the rapid deepening rate and the final depth of the cyclone. The result also points to the importance of incorporating more realistic low-level thermal field into the model initial conditions in order to predict the cyclogenesis at the right time and the right location.

4.2 Numerical predictability

With the above quantitative results in mind, we are ready to pursue the question of the storm's predictability as raised by BS91. In the next, we examine first the effects of the low-level thermal forcing over the ocean using a different set of initial conditions, and then the upper-level forcing by initializing the model 12 h later, on the realistic simulation of the coastal storm. Finally, we discuss how the low- and upper-level interactions determine the final intensity of the storm.

a. Sensitivity to initial thermal uncertainties over the ocean

We have discussed in section 3.1 that when the NMC analysis was used directly as the model input, the MM4 simulates a coastal cyclone that grows from the initial oceanic mesolow rather than from a vorticity center in the frontal zone (Exp. NEH), as did the then operational forecast. As compared to Exp. CTL, the result reveals two basic problems with the initial conditions used in Exp. NEH: i) the poor resolution of the coastal frontal zone, including the low-level vorticity and convergence centers; and ii) the poorly defined low-level thermal forcing over the ocean. The former appears to determine whether or not the coastal cyclone would be spawned from the frontal zone, whereas the latter would affect the initial organization of the coastal cyclogenesis. However, as mentioned in section 2.4, the

low-level thermal structures over the ocean for these simulations have been modified according to the BS91 surface analysis. Thus, another moist sensitivity simulation was conducted, in which the NMC analysis over the ocean were unchanged (Exp. NBG), in order to see how the model simulation is sensitive to the low-level thermal structures in the warm sector.

Fig. 4.4 shows the different initial temperature structures at 900 hPa between the CTL-used (solid) and the NBG-used (dashed). A major difference is the systematic shift of a thermal ridge slightly to the northeast of the CTL-used. With the initial conditions, the model simulates well the development of a cyclone out of the frontal zone, but with a track systematically shifted to the northeast of the CTL-simulated, mostly produced in the first 12-h period (not shown). This shift results in quite different cyclonic circulations at the end of the 24-h integration, although its central pressure is only 1 hPa weaker than the control-simulated. For example, Fig. 4.1b exhibits a broad surface trough offshore with an open isobar into the north. The northward shift of the weaker inshore flow of colder and dryer continental air mass produces much less precipitation in the cold sector; the 24-h accumulated maximum rainfall is 25 mm (not shown) compared to 61 mm in Exp. CTL (see Fig. 3.7b). Again, the weak sensitivity of the simulated central pressure to diabatic heating is evident. The result indicates that i) enhancing the NMC analysis is essential in the generation of the right cyclone system when its signal is weak to begin with; and ii) the model is sensitive to the slight change in the low-level thermal structure in the warm sector as it influences the track, precipitation and circulation characteristics of the coastal cyclone. The importance of the low-level thermal pattern in the cyclogenesis is obvious from a PV-

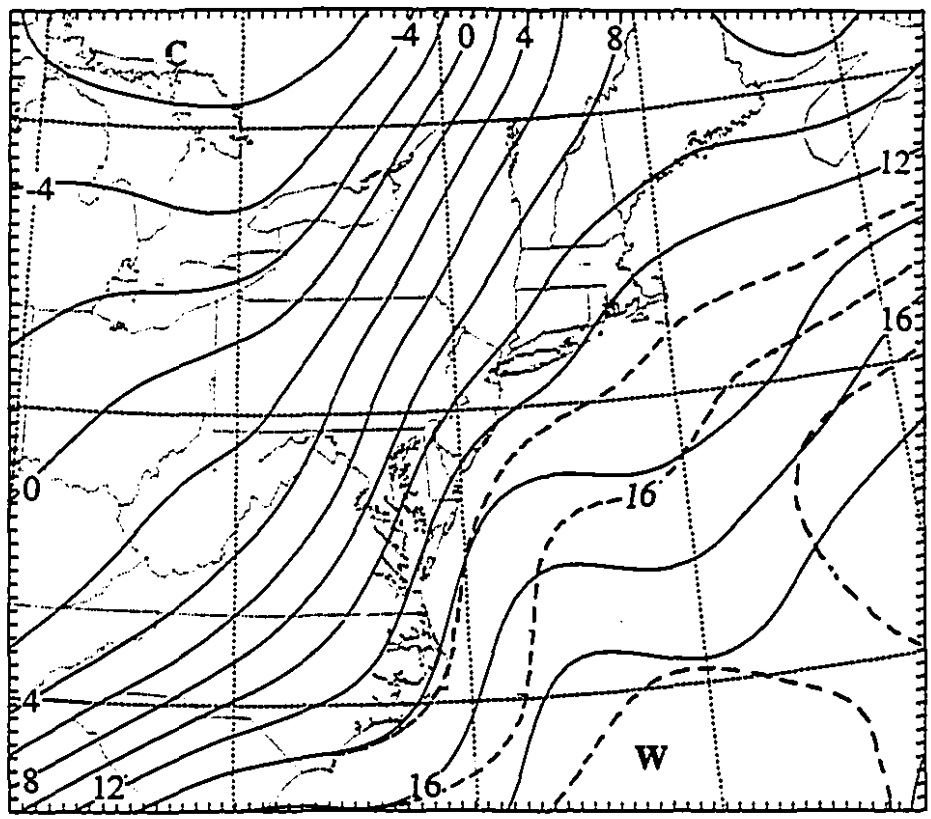

Fig. 4.4 Initial 900-hPa temperature structures for Exps. CTL (solid) and NBG (dashed) at intervals of 2 °C.

inversion viewpoint, since the thermal ridge being modified can be considered as equivalent to a positive PV anomaly contributing to the surface development (Davis and Emanuel 1991).

b. Sensitivity to later initialization

To examine the dominant role of the upper-level forcing in determining the predictability of the coastal cyclogenesis, we conducted a sensitivity experiment, in which the moist model was initiated 12 h later, i.e., at 0000 UTC 4 October (Exp. I12). At this time, the upper-level wave structure was well resolved by the conventional network over the coastal region. However, the flow fields over the ocean still remained poorly defined, as compared to the BS91 analysis, such as the misplaced position of the surface lows, the poorly represented frontal zone and the absence of a low-level thermal ridge and a closed circulation near the cyclone center (not shown).

Despite the poor initial conditions over the ocean, the model reproduces remarkably well the intensification and movement of the coastal cyclone after 6 h into the integration (see Figs. 3.1 and 3.2). The error in position at the end of the 12-h integration is less than 75 km. The model also captures well the deepening rate in the second 6-h simulation, although the final central pressure is about 4 hPa (2 hPa) weaker than the BS91 (NMC) analyzed. In addition, the model produces better the cyclonic and frontal circulation structures than the control-simulated, including the packed isobars in the cold sector, the strong easterly return flow to the north, and the rapid movement of the cold front (cf. Figs. 4.1c and 3.6a, b).

This successful run cannot be attributed simply to the relatively strong signal of the

cyclone at the initial time, since the NGM model, initialized at 0000 UTC 4 October, also predicted a cyclone that grows out of a wrong low-pressure system with a track too far to the east (see Fig. 11 in BS91). Rather, the result reveals that the quasi-geostrophic principle operates more efficiently at the later stages of the cyclone's life cycle, as mentioned earlier. If the initial conditions over the ocean were well represented, the model should be capable of capturing most of the deepening episodes of the storm.

c. Low- and upper-level interaction and the cyclogenesis

We have shown in chapter 3 that with the BS91-suggested improvements of initial conditions over the coastal region and the slight modification in the low-level temperature structure over the ocean (in warm sector), the MM4 does show superior results to the then operational forecast. However, the model still underpredicts the intensity of the storm even when it is initialized 12-h later (e.g., Exp. I12). On the other hand, numerical models often tend to overpredict the development of extratropical cyclones when the initial conditions are well represented (e.g., Mass and Schultz 1993; Huo et al. 1995). This implies that some other factors, which could not be evaluated from the conventional observations, might determine the predictability of the storm at the right depth and the right location. Specifically, after analyzing the vertical PV structures with respect to the surface cyclone (see Figs. 3.10a, b), it is suspected that the simulated weaker cyclone intensity might be related to the coupling of the low- and upper-level PV anomalies.

To see if the above is the case, we need to first obtain a reasonable "ground truth" with which all the simulations could be compared. A more realistic way to achieve this is to perform a dynamic nudging experiment (Exp. NUG) following Stauffer and Seaman

(1990) and Stauffer et al. (1991), in which the 12 hourly enhanced upper-air analyses of winds and temperatures are used to nudge the model integration continuously during the 24-h period (see section 2.3). Since the surface cyclone at 4/12-24 was centered approximately between the two upper-air rawinsonde stations, i.e., Boston (MA) and Portland (ME), this experiment should yield the best possible numerical representation of the coastal cyclone during the mature stage. Indeed, Fig. 4.1d shows several significant improvements over both Exps. CTL and I12 (cf. Figs. 3.6a, b and 4.1c, d). They include i) a more circular shape of isobars; ii) the right position of the surface cyclone center; iii) the right orientation of the cold and warm fronts; iv) the westward extension of the cyclone's influence; and v) a more southeastward extension of the 0^0C isotherm. Although Exp. NUG could not reproduce the (point) minimum surface pressure as observed owing to the nudging toward the upper-level larger-scale analysis, the associated pressure gradients, which determine the intensity of cyclonic circulations, compare favorably to the observed (cf. Figs. 4.1d and 3.6a).

Now, let us examine a vertical cross section of PV and potential temperature from Exp. NUG at 4/12-24 that is taken along a line through the surface cyclone and 300-hPa PV centers. It is evident that the general PV structures are similar between Exps. NUG and CTL (cf. Figs. 4.5 and 3.10b), such as the low-level moist PV concentration and the descending of stratospheric PV-rich air to as low as 600 hPa. The weaker PV anomaly at 350 hPa and ascending motion along the frontal zone are consistent with the simulated weaker surface central pressure, and they can be again attributed to the nudging toward a large-scale upper-air analysis. On the other hand, the stronger low-level PV concentration (> 4 PVUs) results from more intense circulations in conjunction with larger static stability over the cyclone

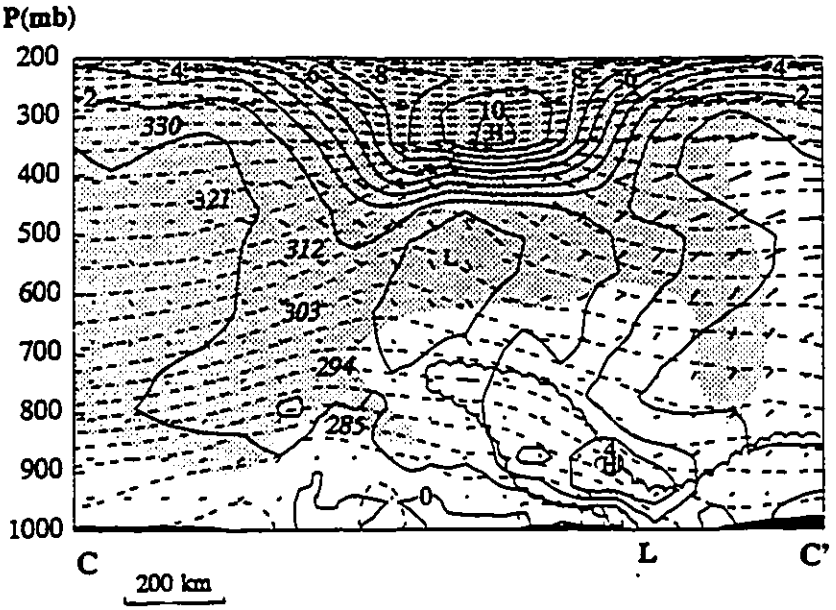

Fig. 4.5 As in Fig. 3.10, but from 24-h integration of Exp. NUG, which is taken along line CC' given in Fig. 4.1d.

center. Of particular relevance here is that the low- and upper-level PV concentrations are well coupled right above the cyclone center through the 2 PVU contour. This is in significant contrast to Exp. CTL (and other sensitivity simulations) in which the upper-level PV anomaly lacks about 150 km behind the surface low at this time. The result appears to imply that the coupling of the upper- and low-level disturbances needs to be reasonably simulated in order to replicate the observed intensity and cyclonic circulations. This explains why all the other sensitivity runs, including the then NGM forecast, simulate poorly the observed intensity of the coastal storm, because the surface lows are always located too far to the northeast or east of the upper-level PV anomaly. Therefore, we may conclude that the initial uncertainties in the low-level temperature structures over the ocean are most likely the cause for the underprediction of the coastal storm, since i) the model resolves well the initial upper-level PV anomaly and simulates reasonably its subsequent movement; ii) most of the error in position occurs during the first 12-h integration in which the thermal forcing dominates; and iii) latent heat release has less significant effect on the cyclogenesis.

Chapter 5 Summary and Concluding Remarks

In this thesis, a series of numerical simulations using the PSU/NCAR MM4 model have been performed to i) investigate the roles of various dynamical and physical processes in the coastal frontal cyclogenesis that occurred during 3-4 October 1987, and ii) examine different parameters in determining the numerical predictability of the coastal storm. Like many other coastal storms, the then operational NMC model failed to predict the development of the cyclone and its associated heavy precipitation. In this study, we first obtained a realistic 24-h simulation of the storm with improved initial conditions and complete physical representations, and then conducted several numerical experiments to study the model's sensitivity to diabatic heating, ice microphysics and different initial conditions.

It is found that the control simulation reproduces reasonably well the track and intensity of the frontal cyclone, the associated precipitation and other surface features, as verified against the BS91 analysis and other available observations. Although the MM4 underpredicts the central pressure by 7 hPa with an error of 180 km in position at the end of the 24-h integration, it simulates correctly the development of the cyclone from a vorticity center in the coastal frontal zone, rather than from an oceanic mesolow as did by the then NMC operational model. Model diagnosis reveals that the coastal cyclogenesis occurs in a favorable large-scale environment with pronounced thermal advection in the lower troposphere and marked PV concentration aloft associated with the tropopause

depression. The transport of warm and moist air from the marine boundary layer by the low-level inshore flow provides the necessary latent energy for the production of the observed heavy precipitation and a variety of weather phenomena.

To isolate the effects of large-scale baroclinicity and diabatic heating on the coastal cyclogenesis, a sensitivity experiment is conducted in which latent heat release is withheld. It is shown that dry dynamics accounts for the genesis, track and a large portion of the final depth of the cyclone, except that the dry cyclone tends to move slower and have smaller horizontal extent than the moist one. The latent heat release is only responsible for 28% of the total deepening of the cyclone. The much less significant effect of latent heat release, as compared to previous explosive cyclogenesis studies, could be attributed to the non-classical distribution of precipitation, i.e., in the northerly return flow in the cold sector. Specifically, the latent heating in the present case produces an elongated PV anomaly in the lower-level cyclonic return flow that tends to be advected southward away from the cyclone center. Thus, from a PV-inversion perspective, the heating-induced PV anomaly has less chance to contribute persistently to the cyclogenesis.

The simplified Zwack-Okossi vorticity equation is then calculated with the dry simulation results to examine the relative importance of the tropopause depression and the lower-level thermal advection in the cyclogenesis. It is found that the low-level thermal advection accounts for 59% of the cyclonic deepening during the incipient stages, whereas the upper-level forcing becomes more and more dominant at later stages, namely, increased from 41% at 4/00-12 to 85% at 4/12-24. Thus, the quasi-geostrophic forcing acts more efficiently during the rapid deepening stages of the cyclone's life cycle. Based on our

simulation results, we may visualize the present cyclogenesis event as follows. The low-level thermal advection helps the vorticity center in the coastal frontal zone to amplify and move slowly offshore under the influence of the upper-level positive vorticity advection during the first 12-h integration. Then, as the upper-level PV anomaly approaches the coastal region, more rapid surface cyclogenesis occurs, leading to the development of intense cyclonic circulations and heavy precipitation.

The impacts of different initial conditions on the cyclogenesis are examined. It is found that the initial uncertainties over the coastal region (e.g., the low-level vorticity center in the frontal zone) determine whether or not the cyclone would develop out of the coastal frontal zone or of an oceanic mesolow. The enhancement of the NMC analysis with all available observations is critical in obtaining the reasonable simulation of the coastal storm. It is also found that the procedure to include the observed surface temperature structure within a deep layer over the ocean in the model initial conditions produces significant influences on the simulated surface features, such as the location of the cyclone center, the intensity, the cyclonic circulation pattern and the precipitation amount. When the model is initialized at 12 h later at which time the upper-level forcing begins to dominate, the model replicates very well the basic circulation features of the system, in spite of the poor-defined surface circulations over the ocean in the initial conditions. This points further to the important role of the quasi-geostrophic processes at later stages in determining the final depth of the coastal cyclone.

While all the simulations mentioned above reproduce to a different degree the basic scenarios of the coastal cyclogenesis event, none of them captures correctly all the observed

features. Thus, a 24-h dynamic nudging experiment is carried out to obtain the "ground truth" of the cyclone's flow structures. Comparisons of this nudging experiment with the other sensitivity simulations reveal that the vertical coupling of the lower- and upper-level PV anomalies is responsible for the underprediction of the cyclone's central pressure as well as its associated circulation structures. This poor coupling is caused by the error in the position of the surface cyclone. That is, the simulated surface cyclones, including the then operational forecasts, are always too far to the east or northeast of the upper-level PV anomaly. It is found that the error in the cyclone's position and the poor coupling can be eventually attributed to the initial low-level thermal uncertainties over the ocean (in the warm sector). Therefore, we may conclude that the then operational failure in predicting the coastal storm was caused by the poor-defined initial conditions in the coastal region as hypothesized by BS91 and the uncertainties of the low-level thermal structures over the ocean. Considering the frequent operational failures in predicting such storms, the above result clearly underlines the importance of incorporating realistic upper-air data over the coastal region into operational model initial conditions in order to improve the quantitative precipitation forecasts and severe weather warnings.

References

Anthes, R. A., and D. Keyser, 1979: Tests of a fine-mesh model over Europe and the United States. *Mon. Wea. Rev.*, **107**, 963-984.

———, and T. T. Warner, 1978: The development of mesoscale models suitable for air pollution and other mesometeorology studies. *Mon. Wea. Rev.*, **106**, 1045-1078.

———, E.-Y. Hsie, and H. L. Kuo, 1987: Description of the Penn State/NCAR mesoscale model version 4 (MM4). NCAR Tech. Note, NCAR/TN-282, 66pp.

———, Y.-H. Kuo and J. R. Gyakum, 1983: Numerical simulations of a case of explosive marine cyclogenesis. *Mon. Wea. Rev.*, **111**, 1174-1188.

Arakawa, A., and V. R. Lamb, 1977: *Computational design of the basic dynamical process of the UCLA general circulation model. Methods in Computational Physics*, **17**, Academic Press, 173-265.

Aubert, E. F., 1957: On the release of latent heat as a factor in large-scale atmospheric motions. *J. Meteor.*, **14**, 527-542.

Benjamin, S. G., and N. L. Seaman, 1985: A simple scheme for objective analyses in curved flow. *Mon. Wea. Rev.*, **113**, 1184-1198.

Bjerknes, J., 1919: *On the structure of moving cyclones.* Geofys. Publ., 1(2), 8pp.

———, and H. Solberg, 1922: *Life cycles of cyclones and the polar front theory of atmospheric circulation.* Geofys. Publ., 3(1), 18pp.

Blackadar, A. K., 1976: Modelling the nocturnal boundary layer. *Preprints Third Symp. on Atmospheric Turbulence, Diffusion and air Quality,* Raleigh, Amer. Meteor. Soc., 46-49.

———, 1979: High resolution models of the planetary boundary layer. *Advances in Environmental Science and Engineering,* 1, No. 1, Pfafflin and Ziegler, eds., Gordon and Breach Sci. Pub., New York, 50-85.

Bosart, L. F., 1975: New England coastal frontogenesis. *Quart. J. Roy. Meteor. Soc.*, **101**, 957-978.

———, 1981: The Presidents' Day storm of 18-19 February 1979: A subsynoptic-scale event. *Mon. Wea. Rev.*, **109**, 1542-1566.

———, and F. Sanders, 1991: An early-season coastal storm: Conceptual success and model failure. *Mon. Wea. Rev.*, **119**, 2831-2851.

———, and S. C. Lin, 1984: A diagnostic analysis of the Presidents' Day storm of February 1979. *Mon. Wea. Rev.*, **112**, 2148-2177.

Brown, J., and K. Campana, 1978: An economical time-differencing system for numerical weather prediction. *Mon. Wea. Rev.*, **106**, 1125-1136.

Carlson, T. N., 1980: Airflow through mid-latitude cyclones and the comma cloud pattern. *Mon. Wea. Rev.*, **108**, 1498-1509.

Chang, C. B., D. J. Perkey, and C. W. Kreitzberg, 1982: A numerical case study of the effects of latent heating on a developing wave cyclone. *J. Atmos. Sci.*, **39**, 1555-1570.

Charney, J. G., 1975: Selected papers of J. A. Bjerknes, *Western Periodicals.*

Chen, S.-J., C. B. Chang, and D. J. Perkey, 1983: Numerical study of an AMTEX'75 oceanic cyclone. *Mon. Wea. Rev.*, **111**, 1818-1829.

Davis, C. A., and K. A. Emanuel, 1991: Potential vorticity diagnostics of cyclogenesis. *Mon. Wea. Rev.*, **119**, 1929-1953.

———, M. T. Stoelinga, and Y.-H. Kuo, 1993: The integrated effect of condensation in numerical simulations of extratropical cyclogenesis. *Mon. Wea. Rev.*, **121**, 2309-2330.

Delsol, F., K. Miyakoda and R. H. Clarke, 1971: Parameterized processes in the surface boundary layer of an atmospheric circulation model. *Quart. J. Roy. Meteor. Soc.*, **97**, 181-208.

Doyle, J. D., and T. T. Warner, 1990: Mesoscale coastal processes during GALE IOP 2. *Mon. Wea. Rev.*, **118**, 283-308.

———, and ———, 1991: A Carolina coastal low-level jet during GALE IOP 2. *Mon. Wea. Rev.*, **119**, 2414-2428.

———, and ———, 1992: A numerical investigation of coastal frontogenesis and mesoscale cyclogenesis during GALE IOP 2. *Mon. Wea. Rev.*, **121**, 1048-1077.

Dudhia, J., 1989: Numerical study of convection observed during the winter monsoon experiment using a mesoscale two-dimensional model. *J. Atmos. Sci.*, **46**, 3077-3107.

Gyakum, J. R., Y.-H. Kuo, Z. Guo, and Y.-R. Guo, 1995: A case of rapid continental mesoscale cyclogenesis. Part II: Model and observational diagnosis. *Mon. Wea. Rev.*,

123, 998-1024.

Hack, and Schubert, 1986: Nonlinear response of atmospheric vortices to heating by organized cumulus convection. *J. Atmos. Sci.*, **43**, 1559-1573.

Harrold, T. W., and K. A. Browning, 1969: The polar low as a baroclinic disturbance. *Quart. J. Roy. Meteor. Soc.*, **95**, 710-723.

Hayden, B. P., 1981: Secular variation in Atlantic coast extratropical cyclones. *Mon. Wea. Rev.*, **109**, 159-167.

Hoskins, B. J., M. E. McIntyre and A. W. Robertson, 1985: On the use and significance of isentropic potential vorticity maps. *Quart. J. Roy. Meteor. Soc.*, **111**, 877-946.

Hsie, E.-Y., R. A. Anthes, and D. Keyser, 1984: Numerical simulation of frontogenesis in a moist atmosphere. *J. Atmos. Sci.*, **41**, 2581-2594.

Huo, Z., D.-L. Zhang, J. R. Gyakum, and A. Staniforth, 1995: A diagnostic analysis of the superstorm of March 1993. *Mon. Wea. Rev.*, **123**, 1740-1761.

Joly, A., and A. J. Thorpe, 1990: Frontal instability generated by tropospheric potential vorticity anomalies. *Quart. J. Roy. Meteor. Soc.*, **116**, 525-560.

Kain, J. S., and J. M. Fritsch, 1990: A one-dimensional entraining/detraining plume model and its application in convective parameterization. *J. Atmos. Sci.*, **47**. 2784-2802.

———, and ———, 1993: Convective parameterization for mesoscale models: The Kain-Fritsch scheme. The Representation of Cumulus Convection in Numerical Models, *Meteor. Monogr.*, No. **46**, Amer. Meteor. Soc., 165-170.

Killworth, P. D., 1980: Barotropic and baroclinic instability in rotating stratifield fluids. *Dyn. Atmos. Ocean*, **4**, 143-184.

Kocin, P. J., and L. W. Uccellini, 1990: Snowstorms along the northeastern coast of the United States: 1955 to 1985. *Meteor. Monogr.*, **22**, No. 44, 280pp.

Kuo, Y.-H., and R. J. Reed, 1988: Numerical simulation of an explosively deepening cyclone in the eastern Pacific. *Mon. Wea. Rev.*, **116**, 2081-2105.

———, J. R. Gyakum, and Z. Guo, 1995: A case of rapid continental mesoscale cyclogenesis. Part I: Model sensitivity experiments. *Mon. Wea. Rev.*, **123**, 970-997.

———, M. A. Shapiro, and E. G. Donall, 1991: The interaction between baroclinic and diabatic processes in a numerical simulation of a rapidly intensifying extratropical

marine cyclone. *Mon. Wea. Rev.*, **119**, 368-384.

Lapenta, W. M., and N. L. Seaman, 1990: A numerical investigation of East Coast cyclogenesis during the cold-air damming event of 27-28 February 1982. Part I: Dynamic and thermodynamic structure. *Mon. Wea. Rev.*, **118**, 2668-2695.

———, and ———, 1992: A numerical investigation of east coast cyclogenesis during the cold-air damming event of 27-28 February 1982. Part II: Importance of physical mechanisms. *Mon. Wea. Rev.*, **120**, 52-76.

Leary, C., 1971: Systematic errors in operational National Meteorological Center primitive equation surface prognoses. *Mon. Wea. Rev.*, **99**, 409-413.

Lupo, A. R., P. J. Smith, and P. Zwack, 1992: A diagnosis of the explosive development of two extratropical cyclones. *Mon. Wea. Rev.*, **120**, 1490-1523.

Mass, C. F. and D. M. Schultz, 1993: The structure and evolution of a simulated midlatitude cyclone over land. *Mon. Wea. Rev.*, **121**, 889-917.

Molinari, J., and M. Dudek, 1992: Parameterization of convective precipitation in mesoscale numerical models: A critical review. *Mon. Wea. Rev.*, **120**, 326-344.

Moore, G. K. W., and W. R. Peltier, 1987: Cyclogenesis in frontal zones. *J. Atmos. Sci.*, **44**, 384-409.

Nitta, T., and Y. Ogura, 1972: Numerical simulation of the development of the intermediate-scale cyclone in a moist model atmosphere. *J. Atmos. Sci.*, **29**, 1011-1024.

Perkey, D. J., and C. W. Kreitzberg, 1976: A time-dependent lateral boundary scheme for limited-area primitive equation models. *Mon. Wea. Rev.*, **104**, 744-755.

Petterssen, S., 1941: Cyclogenesis over southeastern United States and the Atlantic coast. *Bull. Amer. Meteor. Soc.*, **22**, 269-270.

———, 1956: *Weather Analysis and Forecasting*, Vol. I, 2nd Ed., McGraw-Hill, 266-272, 320-339.

Reed, R. J., 1979: Cyclogenesis in polar air streams. *Mon. Wea. Rev.*, **107**, 38-52.

———, M. T. Stoelinga, and Y.-H. Kuo, 1992: A model-aided study of the origin and evolution of the anomalously high potential vorticity in the inner region of a rapidly deepening marine cyclone. *Mon. Wea. Rev.*, **120**, 893-913.

Sanders, F., 1986: Explosive cyclogenesis over the west-central North Atlantic ocean, 1981-

84. Part I: Composite structure and mean behavior. *Mon. Wea. Rev.*, **114**, 1781-1794.

———, 1987: A study of 500 mb vorticity maxima crossing the East Coast of North America and associated surface cyclogenesis. *Wea. Forecasting*, **2**, 70-83.

———, 1987: Skill of NMC operational dynamic models in prediction of explosive cyclogenesis. *Wea. Forecasting*, **2**, 322-336.

———, and J. R. Gyakum, 1980: Synoptic-dynamic climatology of the "bomb.". *Mon. Wea. Rev.*, **108**, 1589-1606.

Simmons, A. J., and B. J. Hoskins, 1976: Baroclinic instability on the sphere: normal modes of the primitive and quasi-geostrophic equations. *J. Atmos. Sci.*, **33**, 1454-1477.

Schär, C., and H. C. Davies, 1990: An instability of mature cold fronts. *J. Atmos. Sci.*, **47**, 929-950.

Sjostedt, D. W., J. T. Sigmon, and S. J. Colucci, 1990: The Carolina nocturnal low-level jet: Synoptic climatology and a case study. *Wea. Forecasting*, **5**, 404-415.

Stauffer D. R., and N. L. Seaman, 1990: Use of four-dimensional data assimilation in a limited-area mesoscale model. Part I: Experiments with synoptic data. *Mon. Wea. Rev.*, **118**, 1250-1277.

———, ———, and F. S. Binkowski, 1991: Use of four-dimensional data assimilation in a limited-area mesoscale model. Part II: Effects of data assimilation within the planetary boundary layer. *Mon. Wea. Rev.*, **119**, 734-754.

———, and T. T. Warner, 1987: A numerical study of Appalachian cold-air damming and coastal frontogenesis. *Mon. Wea. Rev.*, **115**, 799-821.

———, ———, and N. L. Seaman, 1985: A Newtonian "nudging" approach to four-dimensional data assimilation: Use of SESAME-IV data in a mesoscale model. *Preprints, Seventh Conf. on Numerical Weather Prediction*, Montreal, Amer. Meteor. Soc., 77-82.

Thorpe, A. J., 1985: Diagnosis of balanced vortex structure using potential vorticity. *J. Atmos. Sci.*, **42**, 397-406.

Tsou, C.-H., and P. J. Smith, 1990: The role of the synoptic/planetary-scale interactions during the development of a blocking anti-cyclone. *Tellus*, **42A**, 174-193.

Uccellini, L. W., and P. J. Kocin, 1987: The interaction of jet streak circulations during heavy snow events along the east coast of the United States. *Wea. Forecasting*, **2**,

289-308.

———, D. Keyser, K. F. Brill and C. H. Wash, 1985: The Presidents' Day cyclone of 18-19 February 1979: influence of upstream trough amplification and associated tropopause folding on rapid cyclogenesis. *Mon. Wea. Rev.*, **113**, 962-988.

———, P. J. Kocin, R. A. Peterson, C. H. Wash and K. F. Brill, 1984: The Presidents' Day cyclone of 18-19 February 1979: synoptic overview and analysis of the subtropical jet streak influencing the precyclogenetic period. *Mon. Wea. Rev.*, **112**, 31-55.

———, R. A. Peterson, K. F. Brill, P. J. Kocin and J. J. Tuccillo, 1987: Synergistic interactions between an upper-level jet streak and diabatic processes that influence the development of a low-level jet and a secondary coastal cyclone. *Mon. Wea. Rev.*, **115**, 2227-2261.

Whittaker, L. M.,and L. H. Horn, 1981: Geographical and seasonal distribution of North American cyclogenesis, 1958-1977. *Mon. Wea. Rev.*, **109**, 2312-2322.

Zhang, D.-L., 1989: The effect of parameterized ice microphysics on the simulation of vortex circulation with a mesoscale hydrostatic model. *Tellus*, **41A**, 132-147.

———, E.-Y. Hsie and M. W. Moncrieff, 1988: A comparison of explicit and implicit precipitations of convective and stratiform precipitating weather systems with a meso-β-scale numerical model. *Q. J. Roy. Meteor. Soc.*, **114**, 31-60.

———, H.-R. Chang, N. L. Seaman, T. T. Warner, and J. M. Fritsch, 1986: A two-way interactive nesting procedure with variable terrain resolution. *Mon. Wea. Rev.*, **114**, 1330-1339.

———, and J. M. Fritsch, 1986: Numerical simulation of the meso-β scale structure and evolution of the 1977 Johnstown flood. Part I: Model description and verification. *J. Atmos. Sci.*, **43**, 1913-1943.

———, J. S. Kain, J. M. Fritsch, and K. Gao, 1994: Comments on "Parameterization of convective precipitation in mesoscale numerical models: A critical review". *Mon. Wea. Rev.*, **122**, 2222-2231.

———, K. Gao and D. B. Parsons, 1989: Numerical simulation of an intense squall line during 10-11 June 1985 PRE-STORM. Part I: Model verification. *Mon. Wea. Rev.*, **117**, 960-994.

———, and R. A. Anthes, 1982: A high-resolution model of the planetary boundary layer — sensitivity tests and comparisons with SESAME-79 data. *J. Appl. Meteor.* **21**, 1594-1609.